

# Interplay between pairing and triaxial shape degrees of freedom in Os and Pt nuclei

K. Nomura,<sup>1</sup> D. Vretenar,<sup>1,2</sup> Z. P. Li,<sup>3</sup> and J. Xiang<sup>4,3</sup>

<sup>1</sup>*Department of Physics, Faculty of Science, University of Zagreb, HR-10000 Zagreb, Croatia\**

<sup>2</sup>*State Key Laboratory of Nuclear Physics and Technology,*

*School of Physics, Peking University, Beijing 100871, China*

<sup>3</sup>*School of Physical Science and Technology, Southwest University, Chongqing 400715, China*

<sup>4</sup>*School of Physics and Electronic, Qiannan Normal University for Nationalities, Duyun 558000, China*

(Dated: August 23, 2021)

The effect of coupling between pairing and quadrupole triaxial shape vibrations on the low-energy collective states of  $\gamma$ -soft nuclei is investigated using a model based on the framework of nuclear energy density functionals (EDFs). Employing a constrained self-consistent mean-field (SCMF) method that uses universal EDFs and pairing interactions, potential energy surfaces of characteristic  $\gamma$ -soft Os and Pt nuclei with  $A \approx 190$  are calculated as functions of the pairing and triaxial quadrupole deformations. Collective spectroscopic properties are computed using a number-nonconserving interacting boson model (IBM) Hamiltonian, with parameters determined by mapping the SCMF energy surface onto the expectation value of the Hamiltonian in the boson condensate state. It is shown that, by simultaneously considering both the shape and pairing collective degrees of freedom, the EDF-based IBM successfully reproduces data on collective structures based on low-energy  $0^+$  states, as well as  $\gamma$ -vibrational bands.

## I. INTRODUCTION

Ground-state deformations of most medium-mass and heavy nuclei are of quadrupole type, parametrized by the axially-symmetric deformation  $\beta$  (elongation along the symmetry axis of the intrinsic frame), and the degree of triaxiality  $\gamma$  [1]. Quadrupole collectivity is a prominent feature of nuclei, and gives rise to interesting structure phenomena that include (i) quantum (shape) phase transitions [2] that correspond to sudden changes from nearly spherical vibrational to well-deformed rotational nuclear systems by addition or subtraction of just a few nucleons, and (ii) shape coexistence [3] of two or more intrinsic shapes near the ground state in a single nucleus. For an accurate theoretical description of such phenomena, non-axial  $\gamma$  deformations plays a crucial role. In this context, numerous theoretical studies have been carried out from various perspectives [1–9].

In addition to shape degrees of freedom, pairing vibrations play an important role for the structure of heavy nuclei: In particular, for spectroscopic properties of excited  $0^+$  states and the bands built on them, and for electric monopole ( $E0$ ) transitions [1, 10–14]. The relevance of the dynamical pairing degree of freedom in nuclear structure has been recognized since the development of the BCS theory for nuclei in the early 1960s [15–18]. The effect of dynamical pairing and its coupling to the (triaxial) quadrupole shape degrees of freedom has been studied using schematic models (see, e.g., [19–21]). Microscopic models, including those based on the self-consistent mean-field (SCMF) approaches, have also been employed to study the effects of pairing vibrations in various low-energy nuclear structure phenom-

ena and fundamental nuclear processes such as the neutrinoless double- $\beta$  decay, [22] and spontaneous fission [23–26]. All these microscopic studies have been, however, limited to axially symmetric shapes, that is, calculations were performed within a two-dimensional (2D), pairing-plus-axial-quadrupole deformation space. A simultaneous quantitative treatment of pairing and triaxial quadrupole shape deformations, and their explicit coupling in realistic applications, has remained an unsolved problem for nearly sixty years.

In two recent studies we have introduced pairing vibrations as additional building blocks in the quadrupole collective model [27], and the interacting boson model (IBM) [28], based on the framework of nuclear energy density functionals (EDF). It was shown that the inclusion of the dynamical pairing significantly lowers the energies of excited  $0^+$  states in deformed rare-earth nuclei [27, 28]. In Ref. [29] we have extended this framework to include both the triaxial quadrupole shape vibrations and pairing vibrations within the IBM. The method consists of two essential procedures. Firstly, constrained SCMF calculations have been performed using the relativistic mean-field plus BCS (RMF+BCS) method [30] based on the PC-PK1 energy density functional [31], to construct the potential energy surface (PES) as a function of the three-dimensional (3D) quadrupole triaxial and pairing deformations (hereafter denoted as SCMF-PES). In a second step that takes into account both pairing vibrations and triaxiality in spectroscopic calculations, a boson-number-nonconserving Hamiltonian consisting of up to three-body boson terms has been introduced. The parameters of the IBM Hamiltonian are determined in such a way that the SCMF-PES in the vicinity of the global minimum in the 3D-deformation space is mapped onto the expectation value of the Hamiltonian in the boson condensate state (hereafter called IBM-PES). The diagonalization of the mapped IBM Hamiltonian in the

\* knomura@phy.hr

Hilbert space that consists of three subspaces that differ in boson number by one, produces excitation spectra and transition rates. The method has been demonstrated in an illustrative application to the  $\gamma$ -soft nuclei  $^{128}\text{Xe}$  and  $^{130}\text{Xe}$ .

The aim of this work is to investigate in more detail the influence of simultaneously including the pairing and triaxial quadrupole shape vibrations on spectroscopic properties of  $\gamma$ -soft nuclei. Specifically, we give the formulation of the IBM framework within the 3D-deformation space and, in addition to the two cases already considered in Ref. [29] (i.e.,  $^{128,130}\text{Xe}$ ), extend the analysis to the mass  $A \approx 190$  nuclei:  $^{188,190,192}\text{Os}$  and  $^{192,194,196}\text{Pt}$ . The latter is another representative region in which non-axial deformations play an important role. Previous studies within the IBM, based on the relativistic DD-PC1 [32] EDF [33, 34] and the Gogny-D1S [35] and D1M [36] EDFs [37–39], as well as with the five-dimensional collective Hamiltonian based on the relativistic PC-PK1 [40], have shown the importance of triaxiality in the mass  $A \approx 190$  region. An early empirical study [41] presented evidence for a rotor-to-O(6) transition in the Os-Pt region and, in particular, the  $^{196}\text{Pt}$  nucleus was shown to exhibit spectral features predicted in the O(6) dynamical symmetry limit of the IBM [42]. In addition to the PC-PK1 density functional, employed in Refs. [28, 29], here we also consider the DD-PC1 functional for the calculations of the Os and Pt isotopes. By comparing the results obtained with two representative EDFs, we examine the robustness of our method.

The paper is organized as follows. In Sec. II we outline the theoretical method employed in the analysis of spectroscopic properties. The SCMF-PESs and IBM-PESs in the 3D-deformation space are discussed in Sec. III. In Sec. IV we analyze the calculated spectroscopic properties for the nuclei  $^{128,130}\text{Xe}$ ,  $^{188,190,192}\text{Os}$  and  $^{192,194,196}\text{Pt}$ , including low-energy excitation spectra, the effect of coupling pairing and triaxial deformations on excited  $0^+$  states and  $\gamma$ -vibrational bands, a comparison between the PC-PK1 and DD-PC1 functionals, and the  $E2$  and  $E0$  transition rates. Section V contains a summary of the main results and an outline of future research.

## II. METHOD

The SCMF-PESs are computed as functions of the 3D deformations by using the RMF+BCS method [30], with constraints on the mass quadrupole moments and intrinsic pairing deformation. The expectation values of the quadrupole operators  $\hat{Q}_{20} = 2z^2 - x^2 - y^2$  and  $\hat{Q}_{22} = x^2 - y^2$  define the dimensionless polar deforma-

tion parameters  $\beta$  and  $\gamma$ :

$$\beta = \sqrt{\frac{5}{16\pi}} \frac{4\pi}{3} \frac{1}{A(r_0 A^{1/3})^2} \sqrt{\langle \hat{Q}_{20} \rangle^2 + 2 \langle \hat{Q}_{22} \rangle^2} \quad (1)$$

$$\gamma = \arctan \sqrt{2} \frac{\langle \hat{Q}_{22} \rangle}{\langle \hat{Q}_{20} \rangle} \quad (2)$$

with  $r_0 = 1.2$  fm. The expectation value of the monopole pairing operator  $\hat{P} = (1/2) \sum_{k>0} (c_k c_{\bar{k}} + c_{\bar{k}}^\dagger c_k^\dagger)$  in a BCS state (without pairing rotation), where  $k$  and  $\bar{k}$  denote the single-nucleon and the corresponding time-reversed states, respectively, defines the intrinsic pairing deformation parameter  $\alpha$ :

$$\alpha = \sum_{\tau=\pi,\nu} \sum_{k>0} u_k^\tau v_k^\tau, \quad (3)$$

which can be related to the pairing gap  $\Delta$ . To reduce the computational complexity, no distinction is made between proton and neutron pairing degrees of freedom even though, in principle, they should be treated separately. The particle-hole interactions are modeled by the relativistic energy density functionals PC-PK1 [31] and DD-PC1 [32]. For the particle-particle channel, a separable pairing force of finite range [43] is used.

Having computed the 3D SCMF-PES for a given nucleus, in the next step the deformation energy surface is mapped onto the corresponding interacting-boson system [44, 45], using the procedure described below. Here the boson system consists of the monopole  $s$  and quadrupole  $d$  bosons, which, from a microscopic point of view [5, 46], are associated with the correlated  $L = 0^+$  and  $2^+$  pairs of valence nucleons, respectively. To take into account pairing vibrations, the number of bosons  $n$ , which equals half the number of valence nucleons [46], is not conserved, but is allowed to vary by one unit,  $n = n_0, n_0 \pm 1$ . The boson Hilbert space is then expressed as a direct sum of the three subspaces comprising  $n = n_0 - 1, n_0$ , and  $n_0 + 1$   $sd$  bosons

$$(sd)^{n_0-1} \oplus (sd)^{n_0} \oplus (sd)^{n_0+1}. \quad (4)$$

In the following, the three subspaces are simply denoted by  $[n_0 - 1]$ ,  $[n_0]$ , and  $[n_0 + 1]$ . The corresponding IBM Hamiltonian consists of the boson-number conserving (or unperturbed)  $\hat{H}_{\text{cons}}$  and non-conserving  $\hat{H}_{\text{non-cons}}$  interactions:

$$\hat{H} = \hat{H}_{\text{cons}} + \hat{H}_{\text{non-cons}}. \quad (5)$$

To describe structures based on triaxial mean-field minima, it has been shown [34, 47, 48] that it is necessary for the unperturbed Hamiltonian  $\hat{H}_{\text{cons}}$  to contain not only one- and two-body, but also three-body boson terms

$$\hat{H}_{\text{cons}} = \hat{H}_{1b} + \hat{H}_{2b} + \hat{H}_{3b}, \quad (6)$$

where

$$\hat{H}_{1b} = \epsilon_d \hat{n}_d + \hat{\delta} \quad (7a)$$

$$\hat{H}_{2b} = \kappa \hat{Q} \cdot \hat{Q} + \rho \hat{L} \cdot \hat{L} \quad (7b)$$

$$\hat{H}_{3b} = \eta \sum_{\lambda=2,4} ((d^\dagger d^\dagger)^\lambda d^\dagger)^{(3)} \cdot ((\tilde{d}\tilde{d})^\lambda \tilde{d})^{(3)} \quad (7c)$$

with the  $d$ -boson number operator  $\hat{n}_d = \sum_m (-1)^m d_m^\dagger \cdot \tilde{d}_{-m}$  ( $\tilde{d}_{-m} = (-1)^m d_m$ ), the quadrupole operator  $\hat{Q} = s^\dagger \tilde{d} + d^\dagger s + \chi (d^\dagger \tilde{d})^{(2)}$ , and the angular momentum operator  $\hat{L} = \sqrt{10} (d^\dagger \tilde{d})^{(1)}$ . The three-body boson interaction of the form (7c) is shown to be particularly important to produce triaxial minima [34, 47, 48]. We note that for three  $d$  bosons there is only one state with angular momentum  $L = 3$  and, indeed, the terms with  $\lambda = 2$  and  $\lambda = 4$  in Eq. (7c) are proportional to each other. The term  $\hat{\delta} = \epsilon_0 \hat{n} (= \epsilon_0 (s^\dagger s + d^\dagger \cdot \tilde{d}))$  in  $\hat{H}_{1b}$  (7a) determines the relative energies between the three unperturbed  $0^+$  ground states, but does not contribute to the excitation energies within each unperturbed boson subspace. The number-nonconserving Hamiltonian  $\hat{H}_{\text{non-cons}}$  (5) is represented by a monopole-pair transfer operator

$$\hat{H}_{\text{non-cons}} = \theta \frac{1}{2} (s^\dagger + s), \quad (8)$$

where  $\theta$  denotes the strength parameter. The independent parameters of the total boson Hamiltonian (5) are:  $\epsilon_d, \kappa, \chi, \rho, \eta, \theta$ , and  $\epsilon_0$ .

The IBM-PES within the  $(\alpha, \beta, \gamma)$  3D-deformation space is obtained by taking the expectation value of the Hamiltonian in the boson condensate state  $|\Psi(\vec{\alpha})\rangle$  [49–51]

$$|\Psi(\vec{\alpha})\rangle = |\Psi_{n_0-1}(\vec{\alpha})\rangle \oplus |\Psi_{n_0}(\vec{\alpha})\rangle \oplus |\Psi_{n_0+1}(\vec{\alpha})\rangle. \quad (9)$$

The state  $|\Psi_n(\vec{\alpha})\rangle$  for a given subspace comprising  $n$  bosons ( $n = n_0 - 1, n_0, n_0 + 1$ ) is given by

$$|\Psi_n(\vec{\alpha})\rangle = \frac{1}{\sqrt{n!}} (b_c^\dagger)^n |0\rangle, \quad (10)$$

where

$$b_c^\dagger = \frac{1}{\sqrt{\mathcal{N}}} \left[ \alpha_s s^\dagger + \tilde{\beta} \cos \gamma d_0^\dagger + \frac{1}{\sqrt{2}} \tilde{\beta} \sin \gamma (d_{+2}^\dagger + d_{-2}^\dagger) \right] \quad (11)$$

with a normalization factor  $\mathcal{N} = \alpha_s^2 + \tilde{\beta}^2$ . The vector  $\vec{\alpha}$  represents the three amplitudes  $\{\alpha_s, \tilde{\beta}, \gamma\}$ .  $|0\rangle$  is the boson vacuum, that is, the inert core. The IBM-PES is expressed [52] as a  $3 \times 3$  matrix  $\mathbf{E}(\vec{\alpha})$ , with

$$\begin{aligned} E_{n,n}(\vec{\alpha}) &= \langle \Psi_n(\vec{\alpha}) | H_{\text{cons}} | \Psi_n(\vec{\alpha}) \rangle \\ &= a_0 n + n(a_1 + a_2 \tilde{\beta}^2) \mathcal{N}^{-1} \\ &+ n(n-1) [b_1 \alpha_s^2 \tilde{\beta}^2 + b_2 \alpha_s \tilde{\beta}^3 \Gamma + b_3 \tilde{\beta}^4] \mathcal{N}^{-2} \\ &+ dn(n-1)(n-2) \mathcal{N}^{-3} \tilde{\beta}^6 (1 - \Gamma^2) \end{aligned} \quad (12a)$$

for the diagonal elements, and

$$\begin{aligned} E_{n,n'}(\vec{\alpha}) &= E_{n',n}(\vec{\alpha}) = \langle \Psi_{n'}(\vec{\alpha}) | H_{\text{non-cons}} | \Psi_n(\vec{\alpha}) \rangle \\ &= \theta \alpha_s \sqrt{n+1} \mathcal{N}^{-1/2} \end{aligned} \quad (12b)$$

for the off-diagonal ones. Here the shorthand notations  $\Gamma \equiv \cos 3\gamma$ ,  $a_0 = \epsilon_0$ ,  $a_1 = 5\kappa$ ,  $a_2 = \epsilon_d + 6\rho + \kappa(1 + \chi^2)$ ,  $b_1 = 4\kappa$ ,  $b_2 = -4\sqrt{2/7}\kappa\chi$ ,  $b_3 = 2\kappa\chi^2/7$ , and  $d = -\eta/7$  are used. At each  $(\alpha_s, \tilde{\beta}, \gamma)$  coordinate, the matrix  $\mathbf{E}(\vec{\alpha})$  is diagonalized, resulting in three energy surfaces. However, as it is often the case with configuration-mixing IBM calculations that deal with shape coexistence (e.g., Refs. [53–56]), only the lowest eigenvalue at each deformation is considered.

The amplitude  $\tilde{\beta}$  is the IBM analog of the axially symmetric deformation  $\beta$ , while  $\gamma$  represents the degree of triaxiality as usual. The following transformation of the variable  $\alpha_s$  was introduced in [28]:

$$\alpha_s = \cosh(\tilde{\alpha} - \tilde{\alpha}_{\text{min}}). \quad (13)$$

The new coordinate  $\tilde{\alpha}$  is now considered the equivalent quantity to the pairing deformation  $\alpha$ , and  $\tilde{\alpha}_{\text{min}}$  corresponds to the global minimum on the SCMF-PES. The  $\tilde{\beta}$  and  $\tilde{\alpha}$  variables in the boson system can be associated with the deformation parameters in the SCMF model through the relations [28, 29]

$$\tilde{\alpha} = C_\alpha \alpha, \quad \tilde{\beta} = C_\beta \beta, \quad (14)$$

where the constants of proportionality  $C_\alpha$  and  $C_\beta$  are taken as additional parameters to be determined by the mapping. A well-known feature of the IBM is that the energy surface calculated in the condensate state is rather flat for large deformations far from the global minimum, i.e.,  $\beta \gg \beta_{\text{min}}$  and  $\alpha \gg \alpha_{\text{min}}$ . This is a consequence of the fact that the IBM is built on the restricted model space of valence nucleons, whereas the SCMF model considers all nucleons. This difference is partly taken into account by the rescaling relations in (14). The scaling parameters  $C_\alpha$  and  $C_\beta$  should, in principle, be functions of deformations [5], hence we assume that they have the following  $\alpha$  and  $\beta$  dependencies.

$$C'_\beta = C_\beta [\theta(-\beta_*) + \theta(\beta_*) e^{p\beta_*^2}] [\theta(-\alpha_*) + \theta(\alpha_*) e^{q\alpha_*^2}] \quad (15a)$$

$$C'_\alpha = C_\alpha [\theta(-\alpha_*) + \theta(\alpha_*) e^{r\alpha_*^2}] \quad (15b)$$

with  $\alpha_* = \tilde{\alpha} - \tilde{\alpha}_{\text{min}}$  and  $\beta_* = \tilde{\beta} - \tilde{\beta}_{\text{min}}$ , and the step function  $\theta(x) (= 1, \text{ if } x \geq 0 \text{ and } = 0, \text{ if } x < 0)$ . The idea behind the above formulas (15a) and (15b) is that the IBM-PES can be made steeper for large deformations  $\alpha \gg \alpha_{\text{min}}$  and  $\beta \gg \beta_{\text{min}}$ , so that it reproduces the SCMF deformation surface while, for relatively small deformations  $\alpha \leq \alpha_{\text{min}}$  and  $\beta \leq \beta_{\text{min}}$ , the relations in (14) hold, that is,  $C'_\alpha$  and  $C'_\beta$  are constant ( $C'_\alpha = C_\alpha$  and  $C'_\beta = C_\beta$ ). Fixed values are used for the dimensionless coefficients:  $p = 6$ ,  $q = 1$ , and  $r = 0.1$ .

The boson Hamiltonian (5) is determined by applying the procedure of Refs. [28, 29]. First, the parameters of the number-conserving Hamiltonian (6)  $\{\epsilon_d, \kappa, \chi, \eta, C_\beta\}$  are fixed by mapping the SCMF-PES in the 2D  $(\beta, \gamma)$  space with  $\alpha = \alpha_{\min}$  onto the diagonal matrix element associated with the normal  $[n_0]$  configuration  $E_{n_0, n_0}(\alpha_{\min}, \beta, \gamma)$ . Second, the strength parameter  $\rho$  of the term  $\hat{L} \cdot \hat{L}$  is determined separately [57], by equating the bosonic cranking moment of inertia in the intrinsic frame at the global minimum  $(\alpha_{\min}, \beta_{\min}, \gamma_{\min})$  to the corresponding Inglis-Belyaev (IB) value [58, 59] computed using the SCMF quasiparticle states and energies. We note that the IB moment of inertia must be increased by 40 % for Xe and Os nuclei both for the PC-PK1 and DD-PC1 EDFs. This is to take into account the well-known fact that the IB formula underestimates the empirical moments of inertia. Third, the number-nonconserving Hamiltonian (8) is determined in such a way that the SCMF-PES in the 2D  $(\alpha, \beta)$  space with  $\gamma = \gamma_{\min}$  is reproduced by the lowest eigenvalue of the matrix  $\mathbf{E}(\vec{\alpha})$ .

Having thus determined the boson interaction parameters, the mapped IBM Hamiltonian (5) is diagonalized in the model  $\hat{L}$  space defined by Eq. (4).

### III. POTENTIAL ENERGY SURFACES

#### A. 2D projections of SCMF-PESs

The 3D energy surfaces for the Os and Pt isotopes, calculated using the self-consistent RMF+BCS model, are projected onto the 2D  $(\beta, \gamma)$ ,  $(\alpha, \beta)$ , and  $(\gamma, \alpha)$  deformation spaces in Fig. 1 (PC-PK1) and Fig. 2 (DD-PC1), respectively. The 2D projections of the PESs are shown as functions of the axial quadrupole and triaxial deformations  $(\beta, \gamma)$  with fixed  $\alpha_{\min}$ , axial quadrupole and pairing deformations  $(\alpha, \beta)$  with fixed  $\gamma_{\min}$ , and triaxial quadrupole and pairing deformations  $(\gamma, \alpha)$  with fixed  $\beta_{\min}$ . On each surface the fixed values of the deformation parameters correspond to the global minimum in the entire three-dimensional  $(\alpha, \beta, \gamma)$  PES (cf. Table I). Similar contour plots for the nuclei  $^{128, 130}\text{Xe}$  can be found in Ref. [29]. The  $\alpha_{\min}$ ,  $\beta_{\min}$ , and  $\gamma_{\min}$  values for the considered nuclei are listed in Table I. Below we mainly discuss prominent features of the SCMF-PESs calculated with the energy density functional PC-PK1 plus separable pairing, noting the very similar topology of the energy surfaces obtained using the DD-PC1 EDF.

Considering first the  $(\beta, \gamma)$  surfaces, shown in the top row of Fig. 1, the isotopes  $^{188, 190}\text{Os}$  appear to be  $\gamma$ -soft in the interval  $0^\circ \leq \gamma \leq 40^\circ$  and rigid in  $\beta$  deformation. Remarkably, a rigid triaxial minimum is obtained near  $\gamma = 30^\circ$  for the nucleus  $^{190}\text{Os}$ . The three Pt nuclei also exhibit a degree of  $\gamma$ -softness, but are predominantly oblate in shape. The  $(\alpha, \beta)$  energy surfaces, depicted in the middle row of Fig. 1, are notably soft in  $\alpha$  deformation, while rather rigid in the axial  $\beta$  deformation. The  $\alpha$ -

TABLE I. The values  $(\alpha_{\min}, \beta_{\min}, \gamma_{\min})$  of the deformation parameters at which global minima occurs on the 3D energy surfaces, for constrained SCMF calculations based in the functionals PC-PK1 and DD-PC1.

	PC-PK1	DD-PC1
$^{128}\text{Xe}$	(10, 0.20, 18°)	
$^{130}\text{Xe}$	(12, 0.15, 0°)	
$^{188}\text{Os}$	(15, 0.20, 30°)	(9, 0.25, 0°)
$^{190}\text{Os}$	(12, 0.20, 30°)	(6, 0.20, 30°)
$^{192}\text{Os}$	(9, 0.20, 30°)	(6, 0.20, 30°)
$^{192}\text{Pt}$	(18, 0.15, 60°)	(12, 0.20, 36°)
$^{194}\text{Pt}$	(15, 0.15, 42°)	(12, 0.15, 36°)
$^{196}\text{Pt}$	(15, 0.15, 36°)	(12, 0.15, 42°)

softness indicates pronounced pairing fluctuations. The  $\alpha_{\min}$  values for the Pt nuclei are generally larger than those for the Os isotopes. In both Os and Pt nuclei, the equilibrium minimum  $\alpha_{\min}$  in the  $(\alpha, \beta)$  plane gradually decreases with neutron number. In the bottom row of Fig. 1, we note that the SCMF-PESs in the  $(\gamma, \alpha)$  plane show more variation with nucleon number. As one can already infer from the two top rows, the  $(\gamma, \alpha)$  surfaces are soft in both coordinates. Generally, the Os nuclei are more soft in  $\alpha$ , while  $\gamma$ -softness on the oblate side ( $\gamma \approx 60^\circ$ ) is more pronounced in the Pt isotopes.

At the quantitative level, there are certain differences in the topology of the SCMF-PESs obtained using the two functionals. First, in all the 2D-deformation subspaces, the SCMF-PESs calculated with the PC-PK1 EDF are generally softer than those corresponding to the DD-PC1 EDF. For the  $(\alpha, \beta)$  energy surfaces, the PC-PK1 EDF predicts larger equilibrium values  $\alpha_{\min}$  of pairing deformation (see also, Table I). A pronounced difference between the two EDFs is also seen in the  $(\gamma, \alpha)$  plane for the Pt isotopes. It is of interest that the DD-PC1  $(\gamma, \alpha)$ -PESs for the  $^{194, 196}\text{Pt}$  nuclei are softer in  $\gamma$  deformation than those obtained with the PC-PK1 EDF. For  $^{192}\text{Pt}$ , the PC-PK1 SCMF-PES is  $\gamma$  soft, while the one calculated with the DD-PC1 EDF is soft in  $\alpha$  and more rigid in  $\gamma$ .

#### B. 2D SCMF-PESs as functions of the third collective coordinate

It is also of interest to consider, for individual nuclei, the variations of the 2D SCMF-PESs as functions of the third deformation variable. As illustrative examples, we plot in Figs. 3, 4, and 5 the SCMF-PESs for the nuclei  $^{128}\text{Xe}$ ,  $^{188}\text{Os}$ , and  $^{194}\text{Pt}$ , respectively. Here only the results obtained with the functional PC-PK1 are shown. The DD-PC1 results are very similar.

We note some general features of the SCMF-PESs. (i) The  $(\beta, \gamma)$ -PESs for each nucleus become considerably softer as the intrinsic pairing deformation  $\alpha$  is increased.

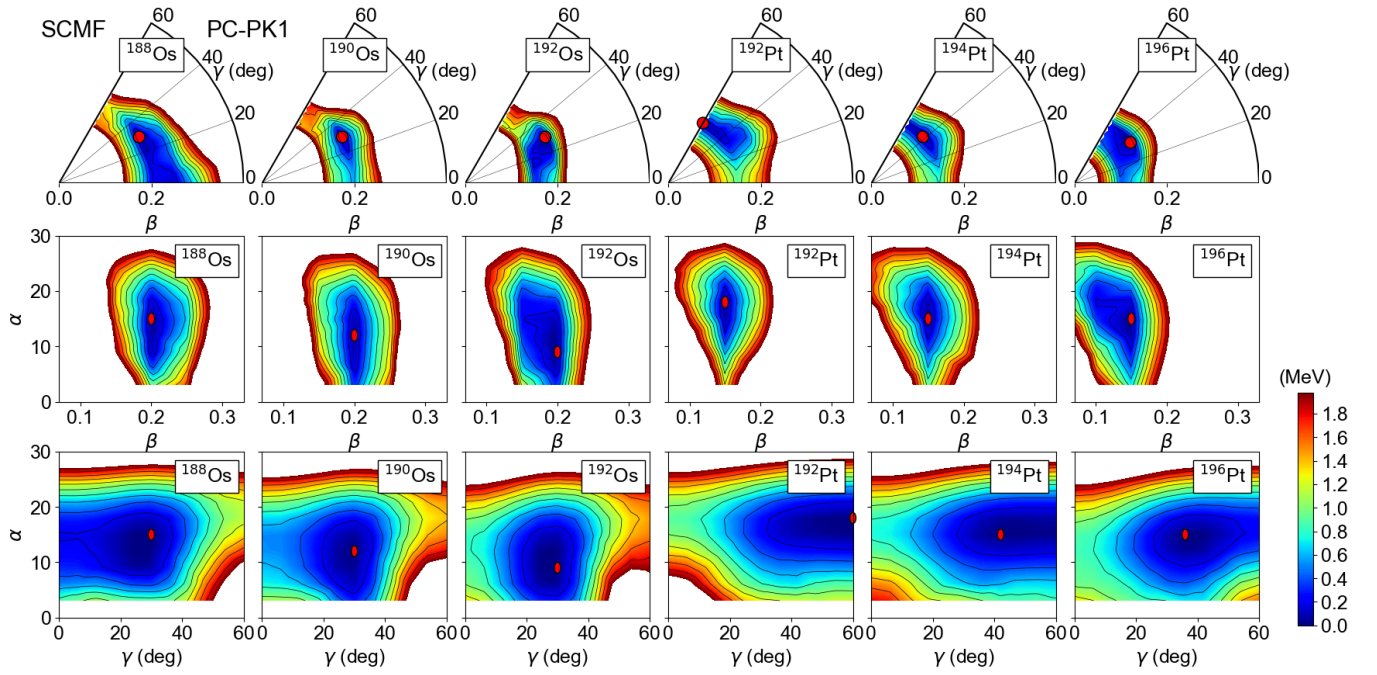


FIG. 1. The SCMF-PESs of  $^{188,190,192}\text{Os}$  and  $^{192,194,196}\text{Pt}$ , projected onto the two-dimensional  $(\beta, \gamma)$  [top],  $(\alpha, \beta)$  [middle], and  $(\gamma, \alpha)$  [bottom] planes (see text for the description). The fixed values of  $\alpha$  in the  $(\beta, \gamma)$ ,  $\gamma$  in the  $(\alpha, \beta)$ , and  $\beta$  in the  $(\gamma, \alpha)$  plots, correspond to the global minimum in the entire three-dimensional  $(\alpha, \beta, \gamma)$  PES (cf. Table I). The PC-PK1 density functional and a separable pairing interaction have been used in the constrained SCMF calculation.

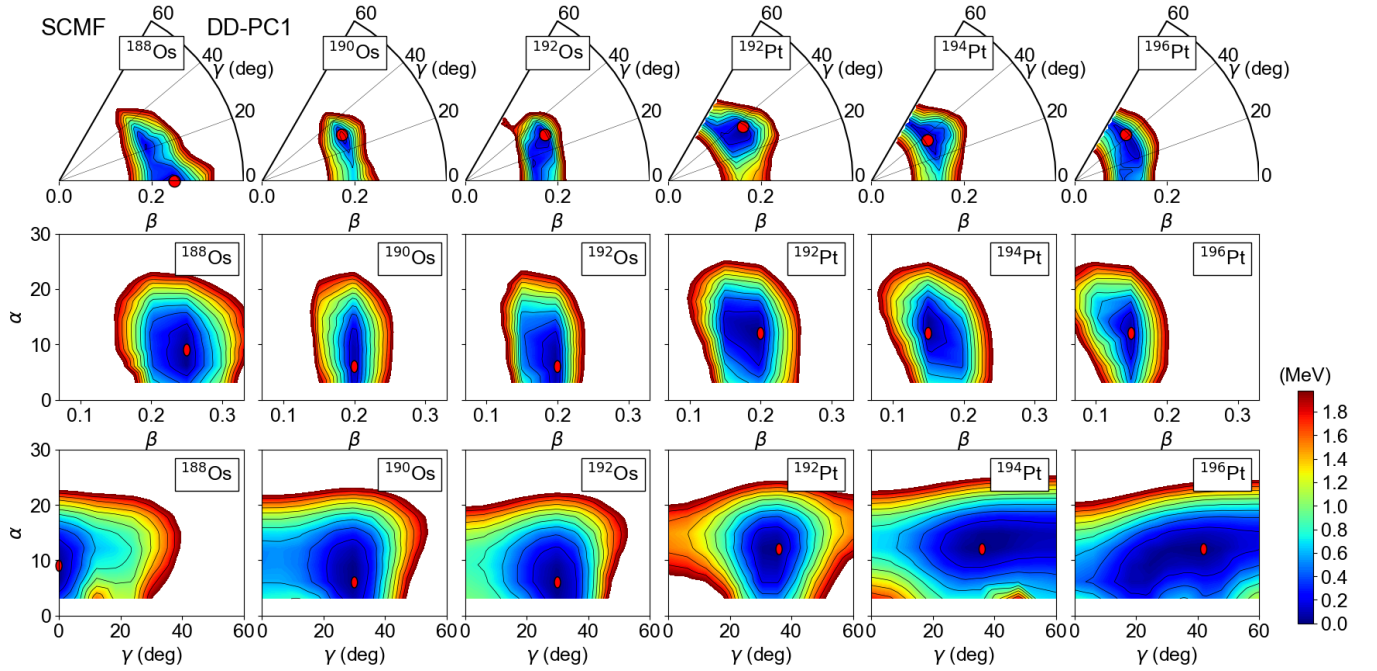


FIG. 2. Same as in the caption to Fig. 1 but for the functional DD-PC1.

This is particularly pronounced for  $^{128}\text{Xe}$  (Fig. 3). (ii) The  $(\alpha, \beta)$  SCMF-PESs are less sensitive to the variation

of the  $\gamma$  deformation, but appear markedly soft near the global minimum corresponding to  $\gamma = \gamma_{\min}$ . (iii) The

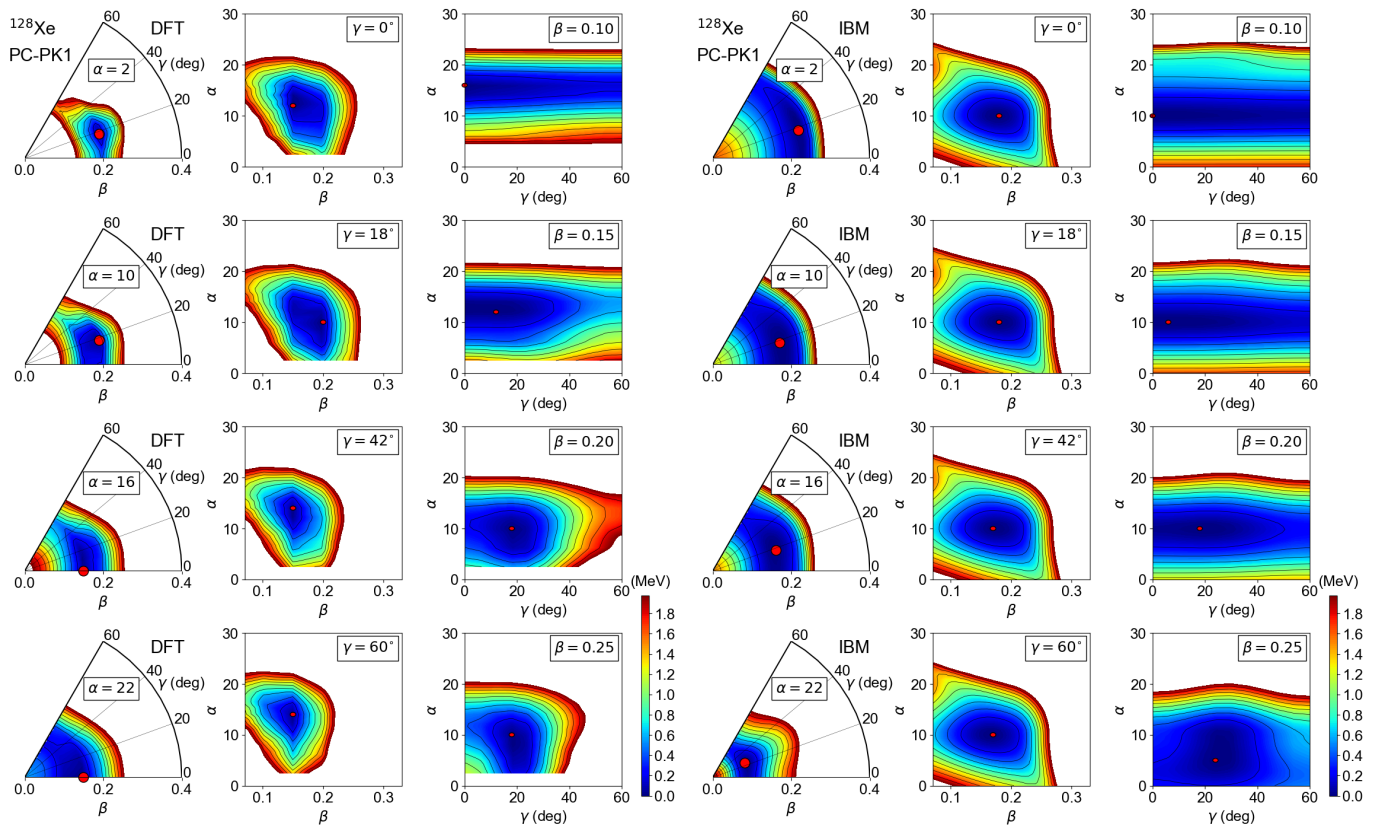


FIG. 3. The SCMF-PESs of  $^{128}\text{Xe}$  projected onto the  $(\beta, \gamma)$  [first column],  $(\alpha, \beta)$  [second column], and  $(\gamma, \alpha)$  planes [third column], as functions of the  $\alpha$ ,  $\gamma$ , and  $\beta$  deformations, respectively. The PC-PK1 density functional and a separable pairing interaction have been used in the constrained SCMF calculation. The corresponding mapped IBM-PESs are plotted on the right hand side (columns 4 – 6).

topology of the  $(\gamma, \alpha)$ -SCMF-PESs varies most rapidly with increasing  $\beta$  values. For small values of  $\beta$ , these 2D surfaces exhibit pronounced  $\gamma$  softness, and become softer in  $\alpha$  with increasing  $\beta$  deformation. Especially near the  $\beta = \beta_{\min}$  equilibrium values, we note a transitional feature, that is, the surfaces are particularly soft with respect to both  $\alpha$  and  $\gamma$ .

### C. Mapped IBM-PESs

From the fourth to the sixth columns of Figs. 3, 4, and 5, we also depict the corresponding IBM-PESs. The variations of these energy surfaces as functions of the parameters  $\alpha$ ,  $\gamma$ , and  $\beta$  on each of the 2D- $(\beta, \gamma)$ ,  $(\alpha, \beta)$ , and  $(\gamma, \alpha)$  deformation spaces, respectively, reproduce those observed for the SCMF-PESs. A notable difference between the SCMF- and IBM-PESs in each 2D space is that the latter are considerably softer with respect to  $\beta$  and  $\gamma$  deformations. As explained in the previous section, such a difference arises because of the restricted (valence) model space of the IBM, compared to that of the SCMF model. Another reason is, apparently, the limited analyt-

ical form of the IBM-PES (12a) and (12b), which does not provide enough variability to accurately reproduce the topology of the SCMF-PES. For example, for general three-body boson terms the energy surface can have a more complicated  $\gamma$  dependence, consisting of terms proportional to  $\beta^3\Gamma$ ,  $\beta^5\Gamma$ , and  $\beta^6\Gamma^2$ , with  $\Gamma = \cos 3\gamma$ . These would imply additional parameters, and thus we use the specific three-body term of the type (7c). On each 2D  $(\beta, \gamma)$  and  $(\gamma, \alpha)$  surfaces, the difference between the SCMF- and IBM-PESs becomes more pronounced as one moves away from the global minimum, because the mapping is considered only in the vicinity of the global minimum. However, these differences should not significantly affect the calculated spectroscopic properties of low-energy collective states.

The parameters of the IBM Hamiltonian (5), as well as the proportionality coefficients  $C_\beta$  and  $C_\alpha$ , for the Xe, Os, and Pt nuclei, obtained using the mapping procedure described in the previous section, are listed in Table II. For both EDFs, most of the parameters appear to be constant or vary only gradually with neutron number in each isotopic chain. It is satisfying that the parameters are only weakly dependent on the nucleon number, be-

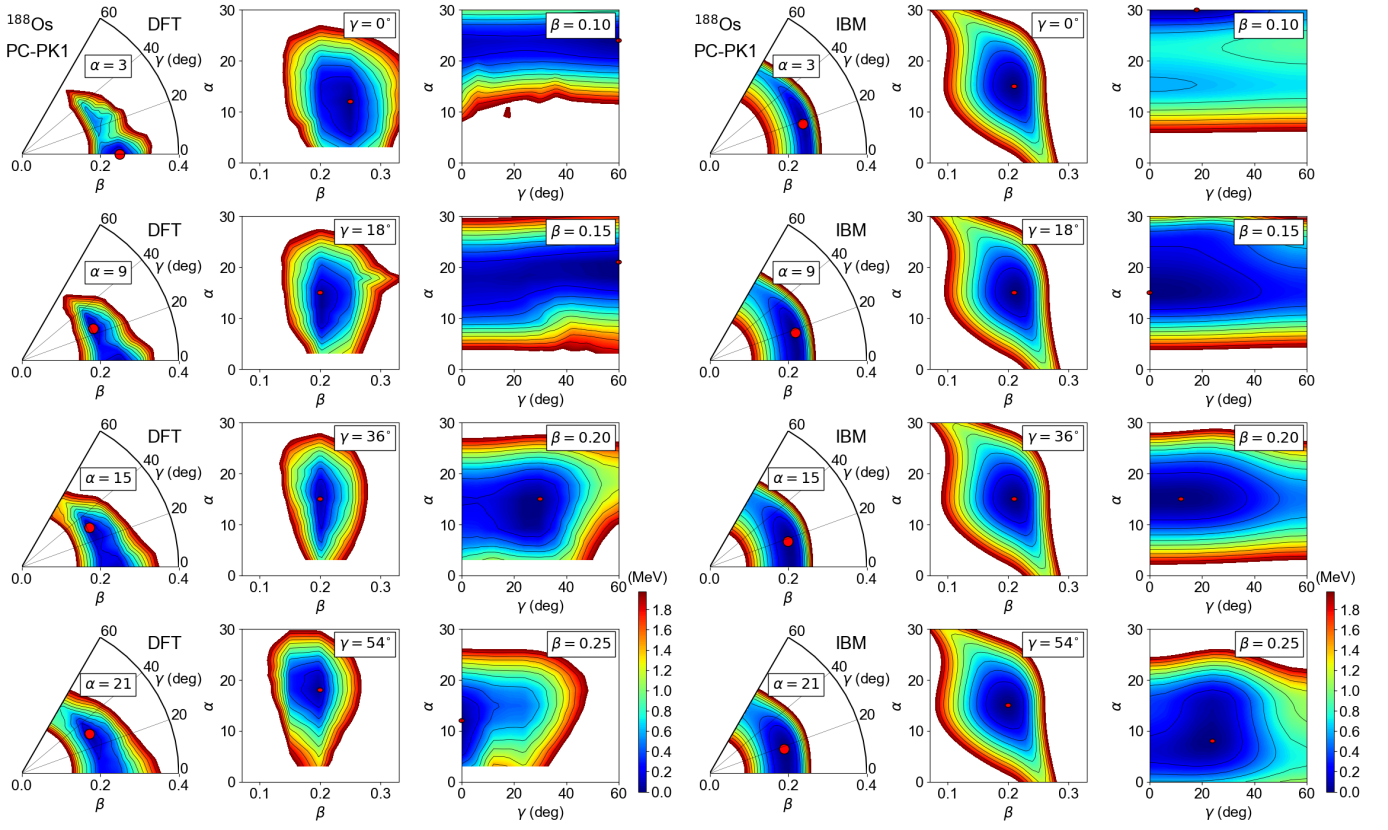


FIG. 4. Same as in the caption to Fig. 3 but for  $^{188}\text{Os}$ .

TABLE II. The values of the IBM Hamiltonian parameters, as well as the constants of proportionality (14), for  $^{128,130}\text{Xe}$ ,  $^{188,190,192}\text{Os}$  and  $^{192,194,196}\text{Pt}$ , determined by the mapping of the PC-PK1 plus separable-pairing self-consistent mean-field results. The corresponding parameters obtained with the DD-PC1 EDF are shown in parentheses.

	$^{128}\text{Xe}$	$^{130}\text{Xe}$	$^{188}\text{Os}$	$^{190}\text{Os}$	$^{192}\text{Os}$	$^{192}\text{Pt}$	$^{194}\text{Pt}$	$^{196}\text{Pt}$
$\epsilon_d$ (keV)	236.5	218.4	117.8 (178.7)	127.4 (191.5)	111.7 (156.8)	200 (249.6)	150 (249.1)	150 (251.5)
$-\kappa$ (keV)	102	102	65 (80)	65 (80)	65 (80)	65 (80)	65 (80)	65 (80)
$\chi$	-0.08	-0.14	-0.1 (-0.2)	-0.02 (-0.025)	-0.02 (-0.05)	0.2 (0.03)	0.03 (0.03)	0.03 (0.08)
$-\rho$ (keV)	15.1	16.1	6.3 (16.4)	7.9 (15.3)	5.3 (9.5)	0.0 (8.3)	0.0 (8.2)	0.0 (8.6)
$\eta$ (keV)	70	100	25 (30)	25 (30)	30 (40)	35 (30)	40 (45)	40 (60)
$\epsilon^0$ (MeV)	1.35	1.3	1.55 (1.95)	1.4 (1.7)	1.3 (1.55)	1.25 (1.5)	1.1 (1.35)	1.0 (1.2)
$\theta$ (keV)	540	740	360 (360)	360 (360)	360 (360)	360 (360)	360 (360)	360 (360)
$C_\beta$	4.0	4.3	4.0 (3.9)	4.1 (4.1)	4.4 (4.4)	5.2 (4.2)	5.0 (4.6)	4.8 (5.0)
$C_\alpha$	0.09	0.095	0.07 (0.07)	0.05 (0.05)	0.07 (0.05)	0.085 (0.06)	0.08 (0.05)	0.09 (0.08)

cause this indicates the consistency of the method and supports the model predictions. The very small values of the parameter  $\chi$  in the quadrupole operator are characteristic for  $\gamma$ -soft nuclei. To simplify the calculation, the mixing strength  $\theta$  is constant ( $\theta = 360$  keV) for all Os and Pt nuclei.

#### IV. SPECTROSCOPIC PROPERTIES

In the remainder of this paper, we will present selected spectroscopic results. Section IV A contains a discussion of low-energy band structure of Os and Pt isotopes, obtained from the 3D-IBM calculations that take into account both the pairing and triaxial degrees of freedom. In Secs. IV B and IV C, we specifically analyze the effect of including dynamical pairing and triaxiality on the

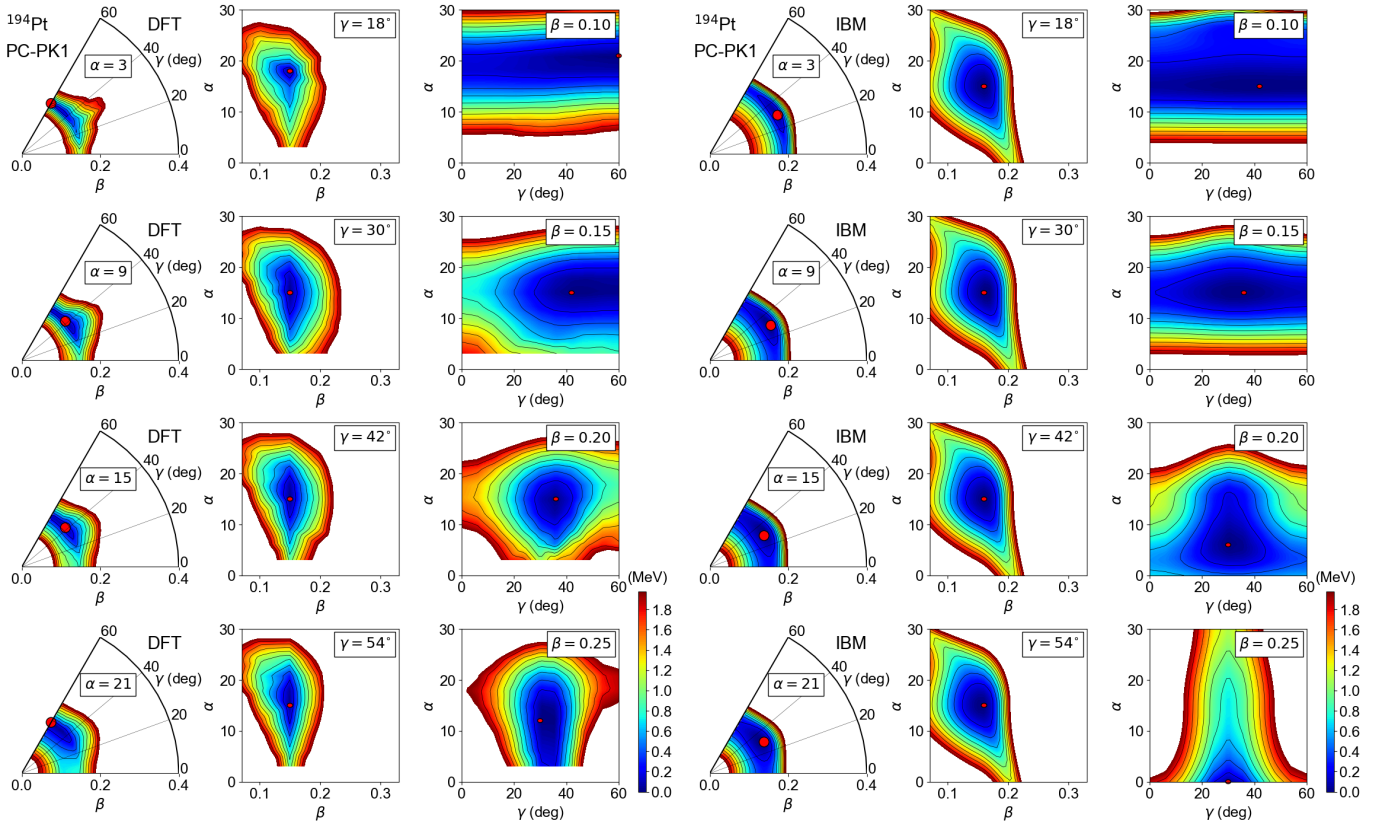


FIG. 5. Same as in the caption to Fig. 3 but for  $^{194}\text{Pt}$ .

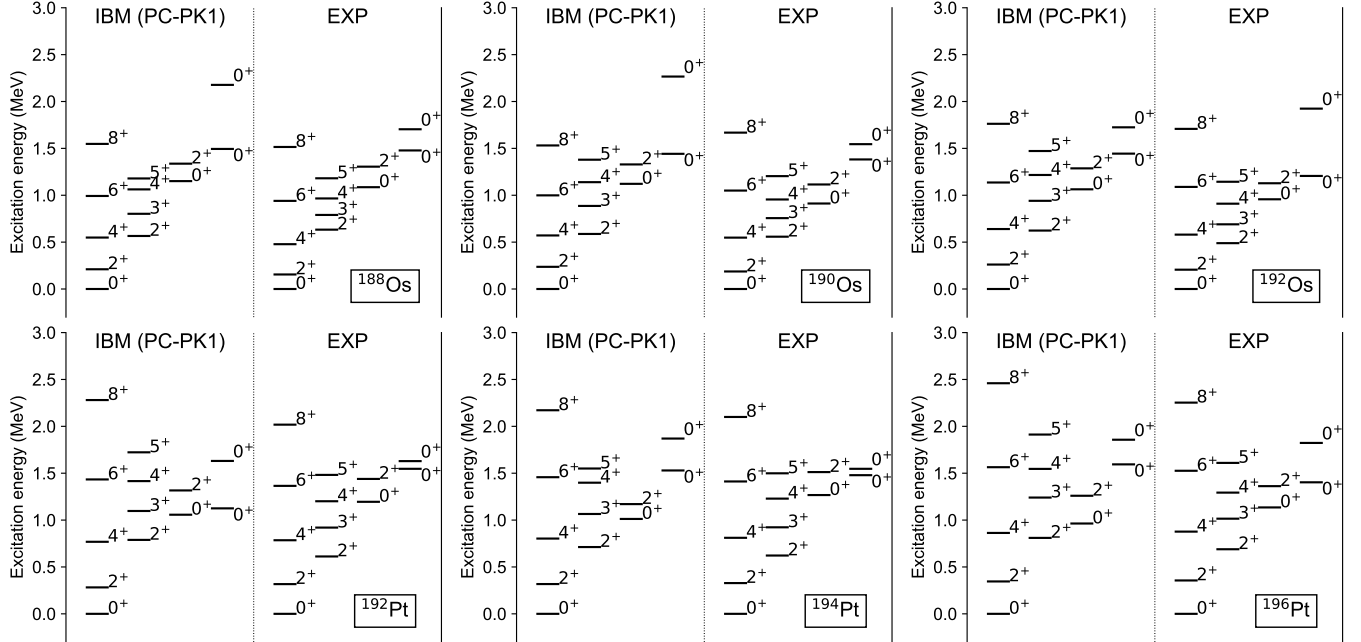


FIG. 6. Comparison of the experimental [60] and theoretical excitation spectra of  $^{188,190,192}\text{Os}$  and  $^{192,194,196}\text{Pt}$ , obtained using the IBM with the triaxial quadrupole ( $\beta, \gamma$ ) plus pairing  $\alpha$  degrees of freedom, and based on the PC-PK1 microscopic energy density functional.

excited  $0^+$  states, and the  $\gamma$ -vibrational band, respectively. Section IV D compares the excitation spectra cal-



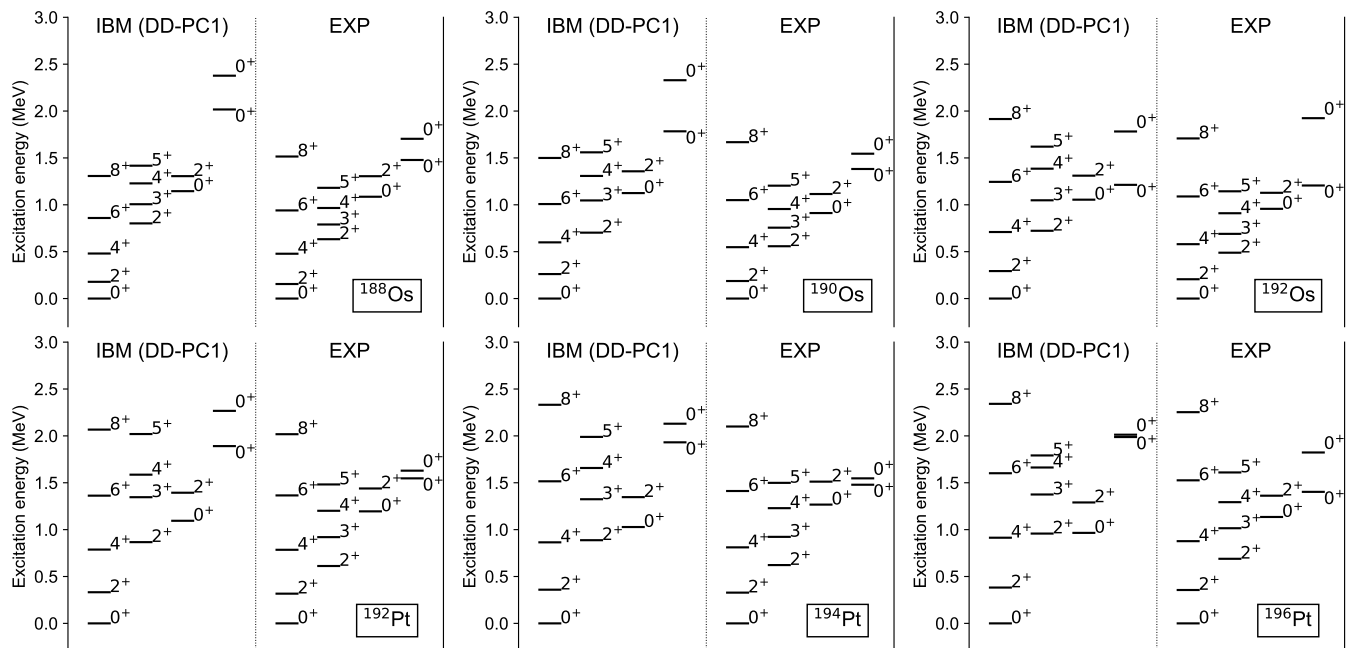


FIG. 7. Same as in the caption to Fig. 6, but the DD-PC1 functional is used to determine the parameters of the IBM Hamiltonian

culated with the PC-PK1 and DD-PC1 energy density functionals. Electric transition properties are discussed in Sec. IV E.

### A. Low-energy excitation spectra

Figures 6 and 7 display the low-energy excitation level schemes of the  $^{188,190,192}\text{Os}$  and  $^{192,194,196}\text{Pt}$  isotopes, calculated with the 3D-IBM based on the PC-PK1 and DD-PC1 EDFs, respectively. In general, the theoretical excitation spectra are in a good agreement with their experimental counterparts [60]. Of particular interest here are the excitation energies of the second  $0^+$  states, which for most of the considered nuclei are predicted very close to the experimental values. In the Os and Pt nuclei analyzed in the present study, as also shown below, the  $0_2^+$  state exhibits a pairing vibrational structure, namely, the principal contributions to this state are from the  $[n_0 \pm 1]$  boson subspaces. The model also predicts the third  $0^+$  levels in agreement with the data, in particular for the calculation based on the PC-PK1 EDF. In many cases one notices that the energy gap between the calculated  $0_3^+$  and  $0_4^+$  levels is much larger than the one observed in experiment, and this strong repulsion between the two  $0^+$  states indicates a high degree of mixing of their wave functions.

The  $\gamma$ -vibrational band, built on the second  $2^+$  state, is overall reproduced in agreement with data, even though the band-head  $2_2^+$  energy is slightly overestimated. Consistent with the experimental sequence, in most cases the

levels of the  $\gamma$  band are almost equidistant. As discussed in more detail in Sec. IV C, this energy-level systematics is characteristic for structures that lie in between those predicted by the rigid-triaxial and  $\gamma$ -unstable rotor geometric models.

By comparing the results shown in Figs. 6 and 7, one notices that the rotational features of the IBM spectra resulting from the DD-PC1 EDF are more pronounced than for those obtained with PC-PK1. For the functional DD-PC1, the  $\gamma$  band is predicted to be higher with respect to the ground-state band, while the  $0_2^+$  band for most of the nuclei is close to or lower than the experimental levels. In the IBM framework, the band-head energies and the moments of inertia of the  $\gamma$ -vibrational band and the band built on the  $0_2^+$  state, are to a large extent determined by the magnitude of the quadrupole-quadrupole interaction strength  $\kappa$  (see, Eq. (7b)). As noted from Table II, the value of  $\kappa$  that is used in the case of the DD-PC1 EDF is more than 20 % larger than for the PC-PK1 case. The different IBM parameters, in turn, reflects the differences in the SCMF-PESs calculated with the two EDFs.

The energy spectra for the Os and Pt nuclei shown in Figs. 6 and 7, are also in better agreement with the data when compared to previous IBM calculations in the Os-Pt region, based either on the Gogny EDFs [37, 38], or the DD-PC1 EDF [33]. In those studies only the two-body IBM Hamiltonian was considered, which resulted in the  $\gamma$  band that exhibits a staggering pattern  $2_\gamma^+$ ,  $(3_\gamma^+, 4_\gamma^+)$ ,  $(5_\gamma^+, 6_\gamma^+)$ , ..., characteristic of the  $\gamma$ -unstable O(6) limit.

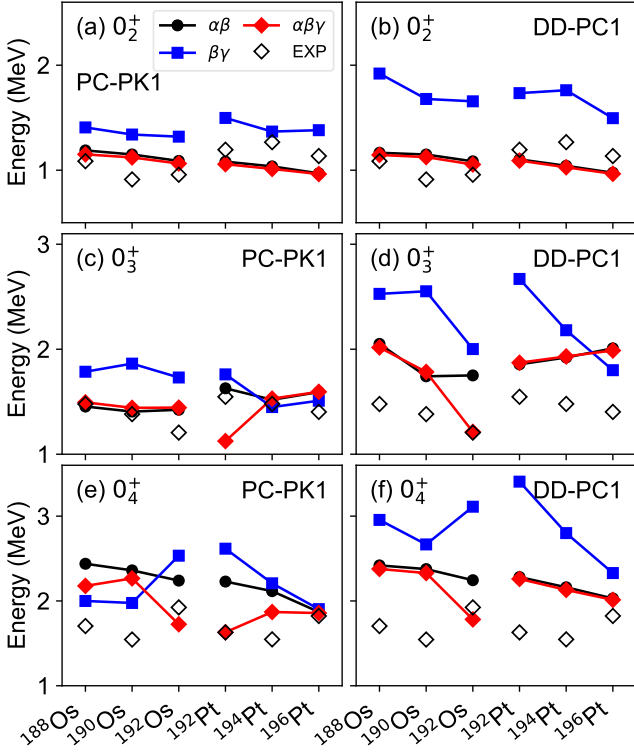


FIG. 8. Excitation energies of the three lowest  $0^+$  excited states in  $^{188,190,192}\text{Os}$  and  $^{192,194,196}\text{Pt}$ , obtained from IBM calculations that include the 2D (triaxial quadrupole  $(\beta, \gamma)$ ), 2D (axial quadrupole  $\beta$  plus pairing  $\alpha$ ), and 3D (triaxial quadrupole  $(\beta, \gamma)$  and pairing  $\alpha$ ) degrees of freedom, in comparison with the corresponding experimental levels.

### B. Effect of dynamical pairing

Figure 8 displays the excitation energies for the second, third, and fourth  $0^+$  states, obtained from IBM calculations that take into account the 2D axial+pairing ( $\alpha\beta$ ), 2D triaxial ( $\beta\gamma$ ), and 3D triaxial+pairing ( $\alpha\beta\gamma$ ) degrees of freedom, respectively. For both Os and Pt isotopes, the  $0_2^+$  energy levels are lowered by a factor of 1.3 – 1.5 with the inclusion of dynamical pairing. The pairing degree of freedom is also relevant for the description of the  $0_3^+$  states in Os isotopes, while for the Pt isotopes it is less significant. Particularly with the PC-PK1 functional, the inclusion of dynamical pairing does not necessarily improve the description of the  $0_4^+$  excitation energies. In the calculation based on the DD-PC1 EDF, dynamical pairing also significantly reduces the  $0_4^+$  excitation energies. In general, it appears that dynamical pairing effects are more pronounced for the case in which the functional DD-PC1 is used as a basis of IBM calculations.

To analyze the structure of  $0^+$  states, we plot in Fig. 9 the percentage of the normal  $[n_0]$  (half the number of valence nucleons), and pair-vibrational  $[n_0 \pm 1]$  components in the IBM wave functions of the four lowest  $0^+$  states.

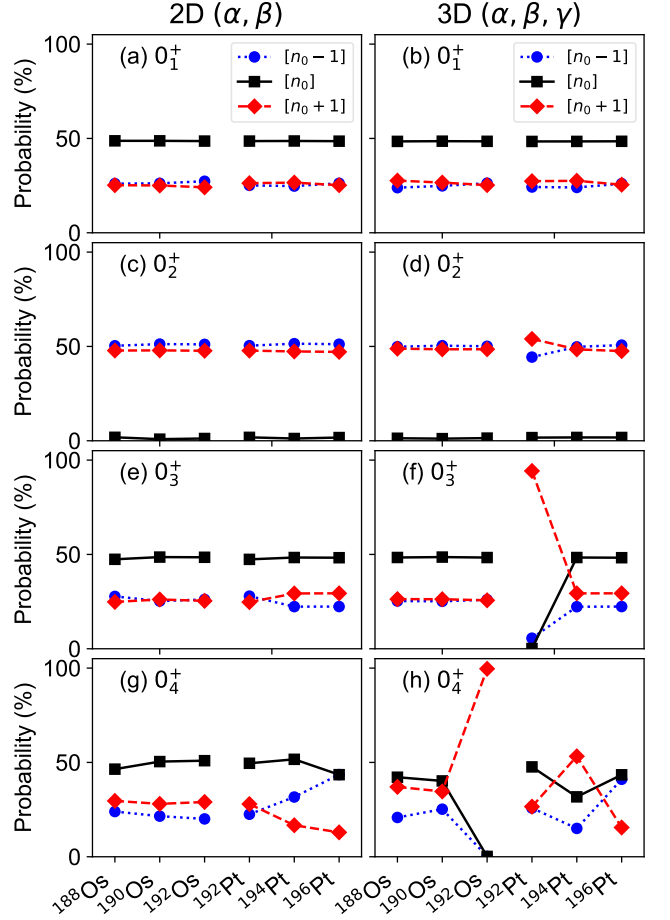


FIG. 9. Fractions of the  $[n_0 - 1]$ ,  $[n_0]$ , and  $[n_0 + 1]$  boson-space components in the wave functions of the four lowest  $0^+$  excited states in  $^{188,190,192}\text{Os}$  and  $^{192,194,196}\text{Pt}$ . These values correspond to the IBM calculations based on the PC-PK1 EDF, and include the 2D (axial quadrupole  $\beta$  plus pairing  $\alpha$ ) (left column), and 3D (triaxial quadrupole  $(\beta, \gamma)$  and pairing  $\alpha$ ) (right column) degrees of freedom.

The 2D- $\alpha\beta$  and 3D- $\alpha\beta\gamma$  IBM results are compared in the left and right columns, respectively. For all the Os and Pt nuclei, approximately 50 % of the wave function of the  $0_1^+$  ground state belongs to the  $[n_0]$  boson space, while the other half is equally shared by the  $[n_0 \pm 1]$  components. For the  $0_2^+$  state, as already noted above, the pair vibrational configurations  $[n_0 \pm 1]$  dominate the corresponding wave function, while the contribution from the  $[n_0]$  space is negligibly small. This conclusion is robust, in the sense that there is no notable difference between the IBM calculations with (3D- $\alpha\beta\gamma$ ) and without (2D- $\alpha\beta$ ) the triaxiality. The same conclusion was drawn for the  $^{128,130}\text{Xe}$  nuclei in [29], and for the axially-deformed rare-earth nuclei in [28]. In Figs. 9(e) to 9(h), the third and fourth  $0^+$  states exhibit structures similar to that of the ground state. Some exceptions occur in the 3D calculation (Figs. 9(f) and 9(h)), for instance, the  $0_3^+$  state

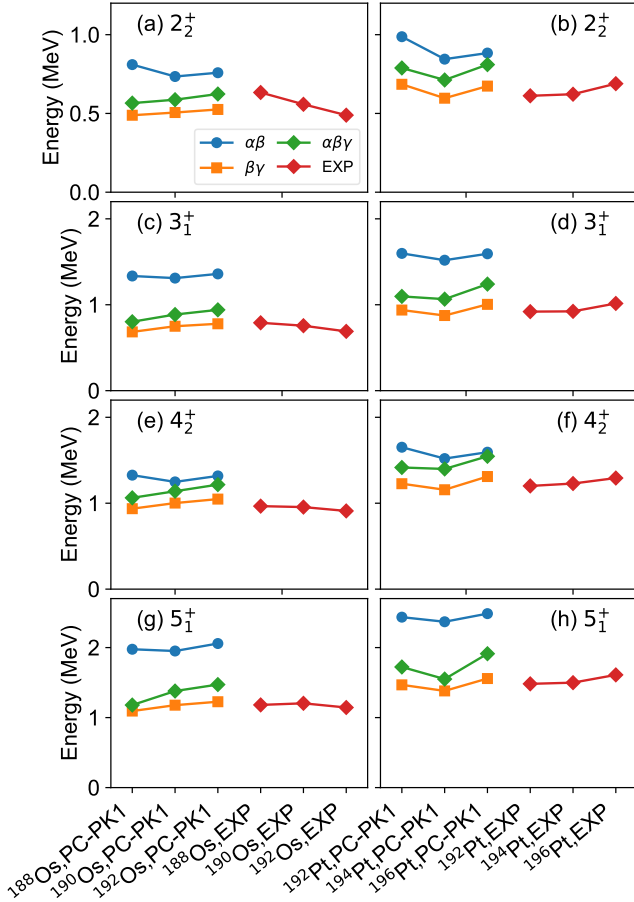


FIG. 10. Excitation energies of  $\gamma$ -band levels of  $^{188,190,192}\text{Os}$  and  $^{192,194,196}\text{Pt}$ , obtained with the IBM that includes the triaxial quadrupole ( $\beta\gamma$ ), axial+pairing ( $\alpha\beta$ ), and triaxial+pairing ( $\alpha\beta\gamma$ ) degrees of freedom, in comparison with the corresponding experimental states. The results based on the functional PC-PK1 are shown.

of  $^{192}\text{Pt}$  and the  $0_4^+$  state of  $^{192}\text{Os}$ . The irregular behavior reflects the complexity of the 3D calculation that involves both triaxial and pairing deformations. A similar conclusion applies to the DD-PC1 results.

### C. Effect of triaxiality

In Fig. 10, the excitation energies of members of the  $\gamma$ -vibrational band of the Os and Pt nuclei are depicted. The theoretical values correspond to the 2D- $\alpha\beta$ , 2D- $\beta\gamma$ , and 3D- $\alpha\beta\gamma$  IBM calculations, respectively, and are shown in comparison to the corresponding experimental levels. As one would expect, the pronounced effect of triaxiality is to lower the excitation energies of the  $\gamma$ -band states, especially the odd-spin ones. The energy levels of the  $\gamma$  band obtained in the 2D- $\beta\gamma$  and 3D- $\alpha\beta\gamma$  calculations are considerably lower than those resulting from

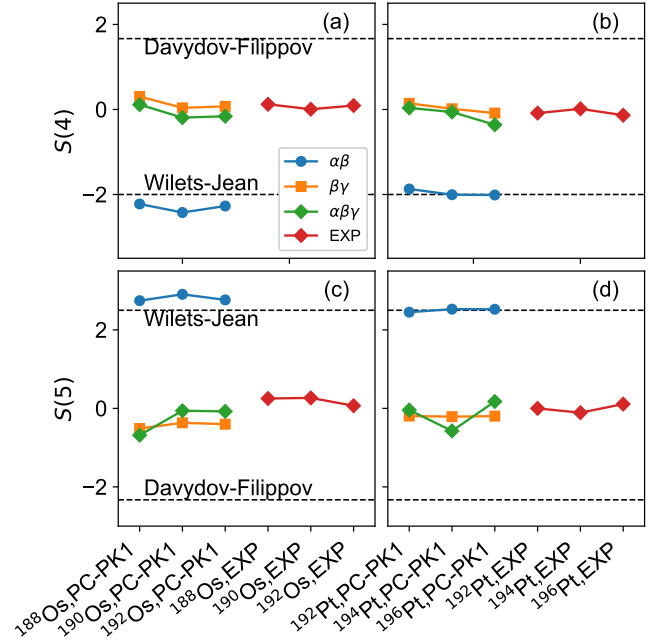


FIG. 11.  $S(4)$  and  $S(5)$  values for the  $\gamma$ -band states of Os (left) and Pt (right) isotopes. The Wilets-Jean limit:  $S(4) = -2.00$  and  $S(5) = 2.50$ , and the Davydov-Filippov limit:  $S(4) = 1.67$  and  $S(5) = -2.33$  are indicated by dashed horizontal lines. The functional PC-PK1 is used in the IBM calculation.

the calculation that includes only axial  $\beta$  and pairing  $\alpha$  deformations. However, it appears that the effect of including dynamical pairing is to slightly raise the  $\gamma$ -band levels, worsening the agreement with available data. The  $\gamma$ -band energies computed with the 3D- $\alpha\beta\gamma$  IBM are systematically higher than those obtained with the 2D- $\beta\gamma$  calculation.

Two limiting geometrical pictures of non-axial nuclei are provided by (i) the rigid-triaxial-rotor model of Davydov and Filippov [61] that corresponds to a collective potential with a stable minimum at a particular value of  $\gamma$ , and (ii) the  $\gamma$ -unstable-rotor model of Wilets and Jean [62] that describes a collective potential that is independent of  $\gamma$ . To distinguish between the energy-level structure of  $\gamma$ -vibrational bands in the two geometrical limits, we consider the quantity  $S(I)$ , defined in terms of the excitation energies of the members of a  $\gamma$  band:

$$S(I_\gamma) = \frac{(E(I_\gamma) - E(I_\gamma - 1)) - (E(I_\gamma - 1) - E(I_\gamma - 2))}{E(2_1^+)} \quad (16)$$

In the ideal  $\gamma$ -unstable-rotor case, its values for  $I_\gamma = 4$  and  $I_\gamma = 5$  are  $S(4) = -2.00$  and  $S(5) = 2.50$ , respectively. These values reflect an approximate grouping pattern  $2_\gamma^+$ ,  $(3_\gamma^+, 4_\gamma^+)$ ,  $(5_\gamma^+, 6_\gamma^+)$ , ... etc. In the rigid-triaxial-rotor limit, the  $S(I)$  values are:  $S(4) = 1.67$  and  $S(5) = -2.33$ , corresponding to the staggering  $(2_\gamma^+, 3_\gamma^+)$ ,

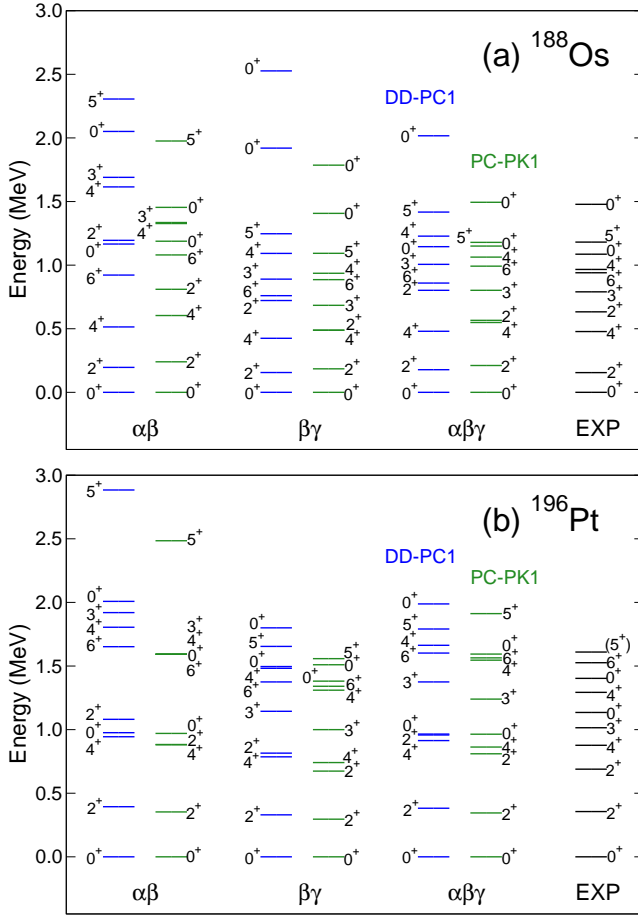


FIG. 12. The low-energy excitation spectra of (a)  $^{188}\text{Os}$  and (b)  $^{196}\text{Pt}$ , obtained from IBM calculations based on the DD-PC1 and PC-PK1 functionals. For each nucleus, results of calculations that include the axial+pairing ( $\alpha\beta$ ), triaxial quadrupole ( $\beta\gamma$ ), and triaxial+pairing ( $\alpha\beta\gamma$ ) deformation degrees of freedom, are compared with experiment.

( $4^+_\gamma, 5^+_\gamma$ ), ... etc.

Figure 11 depicts the values of  $S(4)$  and  $S(5)$  for the Os and Pt nuclei considered in the present study. The 2D- $\alpha\beta$  IBM calculation in all cases predicts the  $S(4)$  and  $S(5)$  values close to the  $\gamma$ -unstable-rotor limit or the O(6) limit of the IBM [5]. This is because any IBM-1 Hamiltonian that includes only two-body boson terms does not give rise to a triaxial minimum, and the resulting  $\gamma$ -band is always that of the  $\gamma$ -unstable-rotor. When triaxiality is taken into account in the 2D- $\beta\gamma$  and 3D- $\alpha\beta\gamma$  calculations, and including the three-body boson term (7c), both  $S(4) \approx S(5) \approx 0$ , a value that is almost halfway between the two geometrical limits. We note that the calculated  $S(4)$  and  $S(5)$  values in the 2D- $\beta\gamma$  and 3D- $\alpha\beta\gamma$  calculations are in very good agreement with the corresponding experimental values. The same conclusion was reached in our previous study of  $^{128,130}\text{Xe}$  [29]. The results for the  $\gamma$ -band obtained with the DD-PC1 EDF are quantitatively similar to those shown in Figs. 10 and

11.

#### D. The DD-PC1 and PC-PK1 excitation spectra

Figure 12 compares the low-energy excitation spectra, calculated using the DD-PC1 and PC-PK1 EDFs to determine the parameters of the IBM Hamiltonian. As examples, we consider the nuclei  $^{188}\text{Os}$  and  $^{196}\text{Pt}$ . A common feature of the two EDFs is that, by the inclusion of dynamical pairing, the excited  $0^+$  states are considerably lowered. Also, when the triaxial degree of freedom is taken into account (that is, the three-body boson interaction is included), states belonging to the  $\gamma$ -band, especially the odd-spin members, are predicted at significantly lower excitation energies. On a closer inspection, it appears that the 3D-IBM calculation based on the PC-PK1 EDF produces results in better quantitative agreement with experiment. As already noted in Sec. IV A, the IBM calculation based on the DD-PC1 functional generally lead to energy spectra that are stretched compared to the PC-PK1 model calculation.

#### E. Transition rates

##### 1. The $E2$ and $E0$ operators

The electric quadrupole ( $E2$ ) and monopole ( $E0$ ) transition rates will also be influenced by the simultaneous inclusion of the quadrupole triaxial and pairing degrees of freedom. An accurate description of these transition rates thus provides a stringent test of the model. The general (one-body)  $E2$  and  $E0$  operators are defined by the following relations:

$$\hat{T}(E2) = e_B \hat{Q} \quad (17)$$

$$\hat{T}(E0) = \xi \hat{n}_d + \zeta \hat{n} \quad (18)$$

where  $e_B$  is the  $E2$  boson effective charge,  $\hat{Q}$  is the same quadrupole operator that appears in the boson Hamiltonian (7b), and  $\xi$  and  $\zeta$  in the  $E0$  operators denote parameters. The  $B(E2)$  and  $\rho^2(E0)$  transition rates are calculated using the expressions:

$$B(E2; I_i \rightarrow I_f) = \frac{1}{2I_i + 1} |\langle I_f || \hat{T}(E2) || I_i \rangle|^2 \quad (19)$$

$$\rho^2(E0; I_i \rightarrow I_f) = \frac{Z^2}{e^2 r_0^4 A^{4/3}} \frac{1}{2I_i + 1} |\langle I_f || \hat{T}(E0) || I_i \rangle|^2. \quad (20)$$

The boson charge  $e_B = 0.145 eb$  is adjusted and kept constant for all the Os and Pt isotopes, and for both the PC-PK1 and DD-PC1 EDFs. This choice for the boson charge ensures that the experimental  $B(E2; 2^+_1 \rightarrow 0^+_1)$  values are reasonably reproduced. In the lighter mass region,  $e_B = 0.12 eb$  is used for  $^{128,130}\text{Xe}$ . The  $E0$  parameters  $\xi = 0.112$  (0.093) and  $\zeta = -0.09$  ( $-0.062$ )  $\text{fm}^2$  are

used for Xe, Os, and Pt nuclei, in calculations with the PC-PK1 (DD-PC1) EDF. These values are determined to reproduce the experimental  $\rho^2(E0; 0_2^+ \rightarrow 0_1^+)$  values of  $^{188}\text{Os}$  and  $^{194}\text{Pt}$  in the 3D-IBM calculation.

It must be noted that, since the boson Hamiltonian consists of up to three-body boson terms, in the calculations that include triaxial degrees of freedom, i.e., the  $(\beta, \gamma)$ - and  $(\alpha, \beta, \gamma)$ -IBM, the  $E2$  operator should also contain higher-order terms:

$$\begin{aligned} \hat{T}(E2) = & e_{sd}(s^\dagger \tilde{d} + d^\dagger s) + e_{dd}(d^\dagger \tilde{d})^{(2)} \\ & + e_{sddd} \sum_{L=0,2,4} \{[(s^\dagger \tilde{d})(d^\dagger \tilde{d})^{(L)}]^{(2)} + (h.c.)\} \\ & + e_{dddd} \sum_{L,L'=0,2,4} [(d^\dagger d^\dagger)^{(L)}(\tilde{d}\tilde{d})^{(L')}]^{(2)}. \end{aligned} \quad (21)$$

with additional boson effective charges  $e_{sd}$ ,  $e_{dd}$ ,  $e_{sddd}$ , and  $e_{dddd}$ . The  $B(E2)$  transition rates calculated by using the two-body  $E2$  operator for the  $^{128,130}\text{Xe}$  can be found in Fig. 4 of Ref. [29]. The  $E2$  charges for the operator (21) chosen for  $^{128}\text{Xe}$  ( $^{130}\text{Xe}$ ) in [29] were  $e_{sd} = 0.078$  (0.09),  $e_{dd} = 0.034$  (0.086),  $e_{sddd} = 0.016$  (0.015), and  $e_{dddd} = 0.009$  (0) eb. To keep the calculation and discussion as simple as possible, in this work we use the standard  $E2$  operator in (17) for all considered nuclei.

In addition, the  $E2$  effective boson charge  $e_B$  and the parameters  $\xi$  and  $\zeta$  in the  $E0$  operator could, in principle, differ in the three boson subspaces  $[n_0]$  and  $[n_0 \pm 1]$ . Again, for simplicity, we use the same values of these parameters for the three configuration spaces, just as in the case of the Hamiltonian parameters.

## 2. $E2$ transition properties

For the Xe, Os, and Pt nuclei considered in this study, a wealth of experimental information on  $E2$  transition rates is available. Tables III, IV, and V compare the experimental [60] and theoretical  $B(E2)$  reduced transition probabilities (in Weisskopf units) for the Xe, Os, and Pt isotopes, respectively. In the tables the theoretical values correspond to IBM calculations that include triaxial quadrupole ( $\beta\gamma$ ), axial plus dynamical pairing ( $\alpha\beta$ ), and triaxial plus dynamical pairing ( $\alpha\beta\gamma$ ) degrees of freedom.

In Table III, it is interesting to note that the inclusion of the pairing degree of freedom has the effect of slightly increasing the  $B(E2; 0_2^+ \rightarrow 2_1^+)$  values for both  $^{128}\text{Xe}$  and  $^{130}\text{Xe}$ . This is seen from the comparison of the 2D- $\beta\gamma$  and the 3D- $\alpha\beta\gamma$  results. This increase in the  $E2$  transition rates is a consequence of configuration mixing between the three boson subspaces, resulting in a larger overlap between initial and final state wave functions. By comparing the 2D- $\alpha\beta$  results with those obtained from the 2D- $\beta\gamma$  or 3D- $\alpha\beta\gamma$  IBM calculations, one notices that the inclusion of the triaxial degree of freedom has a marked effect on the  $E2$  rates that involve members of the  $\gamma$  band. The most prominent example is the increase of the  $B(E2; 3_1^+ \rightarrow 2_2^+)$  values. Note that,

TABLE III. Comparison of experimental [60] and theoretical  $B(E2; I_i \rightarrow I_f)$  values (in Weisskopf units) for  $^{128,130}\text{Xe}$ . The theoretical values are obtained from IBM calculations that include triaxial quadrupole (denoted by  $\beta\gamma$ ), axial plus dynamical pairing ( $\alpha\beta$ ), and triaxial plus dynamical pairing ( $\alpha\beta\gamma$ ) degrees of freedom. The numbers in parentheses for the 2D- $\beta\gamma$  and 3D- $\alpha\beta\gamma$  calculations denote values that are obtained using the two-body  $E2$  operator in Eq. (21). The IBM calculations are based on the PC-PK1 energy density functional.

	$I_i$	$I_f$	EXP	$\beta\gamma$	$\alpha\beta$	$\alpha\beta\gamma$
$^{128}\text{Xe}$	$2_1^+$	$0_1^+$	$42.6 \pm 6.4$	45 (50)	44	46 (49)
	$4_1^+$	$2_1^+$	$63.5 \pm 5.2$	59 (85)	60	61 (82)
	$6_1^+$	$4_1^+$	$106 \pm 13$	60 (95)	62	65 (96)
	$2_2^+$	$2_1^+$	$50.1 \pm 9.7$	54 (48)	25	57 (52)
		$0_1^+$	$0.65 \pm 0.08$	0.29 (11)	2.6	0.22 (9.8)
	$3_1^+$	$4_1^+$	$31.8 \pm 5.9$	20 (19)	11	23 (23)
		$2_2^+$	$91 \pm 16$	49 (63)	12	57 (75)
		$2_1^+$	$1.45 \pm 0.26$	0.39 (8.1)	37	0.33 (9.6)
	$4_2^+$	$4_1^+$	$30.2 \pm 3.2$	23 (31)	6.5	21 (30)
		$2_2^+$	$29.6 \pm 2.9$	28 (23)	21	27 (28)
		$2_1^+$	$0.52 \pm 0.06$	0.0056 (54)	0.042	0.020 (47)
	$0_2^+$	$2_2^+$	$52.8 \pm 0.7.6$	40 (40)	30	0.19 (19)
		$2_1^+$	$3.69 \pm 0.58$	0.37 (115)	4.0	3.8 (16)
	$0_3^+$	$2_2^+$	$22.2 \pm 4.6$	0.37 (73)	33	35 (38)
		$2_1^+$	$10.4 \pm 2.3$	0.28 (12)	0.62	0.30 (101)
	$^{130}\text{Xe}$	$2_1^+$	$0_1^+$	$33.2 \pm 2.6$	33 (42)	32
$4_1^+$		$2_1^+$	$46.4 \pm 4.6$	42 (70)	43	42 (60)
$6_1^+$		$4_1^+$	$69 \pm 9$	41 (78)	43	42 (73)
$2_2^+$		$2_1^+$	$40_{-7}^{+10}$	35 (39)	16	38 (42)
		$0_1^+$	$0.27_{-0.05}^{+0.07}$	0.34 (4.1)	1.8	0.18 (3.4)
$3_1^+$		$4_1^+$	$< 270$	13 (16)	7.5	14 (19)
		$2_2^+$	$57_{-42}^{+59}$	33 (56)	22	37 (61)
		$2_1^+$	$1.0_{-0.7}^{+1.0}$	0.43 (2.4)	3.4	0.26 (2.0)
$4_2^+$		$4_1^+$	$42_{-35}^{+48}$	14 (25)	5.1	14 (26)
		$2_2^+$	$69_{-57}^{+65}$	17 (21)	17	18 (15)
		$2_1^+$	$2.1_{-1.7}^{+2.0}$	0.016 (21)	0.024	0.029 (22)
$0_2^+$		$2_2^+$	$120_{-70}^{+110}$	23 (48)	36	0.39 (19)
		$2_1^+$	$18_{-11}^{+17}$	0.65 (78)	4.5	2.7 (19)
$0_3^+$		$2_2^+$	$55_{-33}^{+37}$	2.5 (6.1)	5.6	0.45 (1.3)
		$2_1^+$		0.17 (6.1)	0.024	1.5 (7.2)

in the 3D- $\alpha\beta\gamma$  IBM results for  $^{130}\text{Xe}$ , the low-spin members of the  $\gamma$  band are the  $2_2^+$ ,  $3_1^+$ ,  $4_3^+$ , and  $5_1^+$  levels. Thus in Table III, the experimental  $B(E2; 4_2^+ \rightarrow I_f)$  are actually compared with the theoretical  $B(E2; 4_3^+ \rightarrow I_f)$  values. For the ground-state band, neither triaxiality nor dynamical pairing degree of freedom has any effect on the in-band  $E2$  transition rates.

For  $^{128,130}\text{Xe}$ , the  $B(E2)$  values for the 2D- $\beta\gamma$  and 3D- $\alpha\beta\gamma$  IBM calculations that employ the two-body  $E2$  operator (21) are also included (values in parentheses in Table III). These values are from Ref. [29]. With the inclusion of the higher-order terms and hence additional adjustable parameters, the  $B(E2)$  values calculated with the two-body  $E2$  operator (21), in some cases agree better with the data, compared to those obtained with only

TABLE IV. Same as in the caption to Table III but for the Os nuclei. Only results calculated with the one-body  $E2$  operator are shown.

	$I_i$	$I_f$	EXP	$\beta\gamma$	$\alpha\beta$	$\alpha\beta\gamma$	
$^{188}\text{Os}$	$2_1^+$	$0_1^+$	$77.5\pm 1.0$	88	89	89	
	$4_1^+$	$2_1^+$	$133\pm 8$	123	125	125	
	$6_1^+$	$4_1^+$	$138\pm 8$	139	139	142	
	$2_2^+$	$2_1^+$	$16.2\pm 1.8$	80	81	85	
		$0_1^+$	$5.0\pm 0.6$	3.1	3.0	2.9	
	$3_1^+$	$4_1^+$		52	32	51	
		$2_2^+$		129	97	130	
		$2_1^+$		5.0	4.6	4.7	
	$4_2^+$	$6_1^+$	$15\pm 6$	2.0	1.0	1.1	
		$4_1^+$	$19\pm 3$	35	49	22	
		$3_1^+$		27	11	14	
		$2_2^+$	$47\pm 8$	45	72	29	
		$2_1^+$	$1.31\pm 0.19$	0.4	0.03	0.14	
	$0_2^+$	$2_2^+$	$4.8\pm 0.3$	36	5.4	$7.0 \times 10^{-4}$	
		$2_1^+$	$0.96\pm 0.05$	1.5	2.9	2.6	
	$0_3^+$	$2_2^+$		$2.3 \times 10^{-5}$	125	46	
		$2_1^+$		0.016	2.2	1.4	
	$^{190}\text{Os}$	$2_1^+$	$0_1^+$	$72.9\pm 1.6$	75	75	75
		$4_1^+$	$2_1^+$	$99^{+5}_{-3}$	102	103	103
		$6_1^+$	$4_1^+$	$113\pm 7$	114	113	115
			$4_2^+$	$5.6^{+4.5}_{-3.6}$	0.051	0.023	0.041
		$2_2^+$	$2_1^+$	$32.6\pm 3.4$	99	101	101
			$0_1^+$	$6.0\pm 0.6$	0.12	0.10	0.10
		$3_1^+$	$4_1^+$		46	32	44
		$2_2^+$		103	80	103	
		$2_1^+$		0.19	0.15	0.16	
$4_2^+$		$6_1^+$		0.074	0.033	0.060	
		$4_1^+$	$31\pm 5$	36	53	40	
		$3_1^+$	$54^{+24}_{-19}$	0.93	0.33	0.72	
		$2_2^+$	$52.3\pm 4.3$	47	59	50	
		$2_1^+$	$0.69\pm 0.06$	0.018	0.0002	0.009	
$0_2^+$		$2_2^+$	$24^{+10}_{-7}$	47	0.20	0.012	
		$2_1^+$	$2.4^{+0.8}_{-0.6}$	0.078	2.0	2.5	
$0_3^+$		$2_2^+$		2.2	0.016	0.0007	
		$2_1^+$		125	$2.3 \times 10^{-5}$	2.6	
$^{192}\text{Os}$		$2_1^+$	$0_1^+$	$62.1\pm 0.7$	61	60	61
		$4_1^+$	$2_1^+$	$75.6\pm 2.0$	81	82	82
		$6_1^+$	$4_1^+$	$100^{+5}_{-3}$	89	88	90
		$2_2^+$	$2_1^+$	$46.0^{+2.6}_{-1.2}$	79	81	81
			$0_1^+$	$5.62^{+0.21}_{-0.12}$	0.072	0.055	0.056
		$3_1^+$	$4_1^+$	36	25	34	
		$2_2^+$	81	63	80		
		$2_1^+$	0.11	0.079	0.085		
	$4_2^+$	$6_1^+$		0.043	0.015	0.032	
		$4_1^+$	$30.9^{+3.6}_{-1.8}$	28	42	32	
		$3_1^+$		0.61	0.16	0.44	
		$2_2^+$	$45.2^{+1.4}_{-1.8}$	36	46	39	
		$2_1^+$	$0.29\pm 0.03$	0.013	$2.0 \times 10^{-5}$	0.0053	
	$0_2^+$	$2_2^+$	$30.4^{+3.0}_{-2.3}$	37	0.097	0.010	
		$2_1^+$	$0.57\pm 0.12$	0.050	2.0	2.5	
	$0_3^+$	$2_2^+$		0.0017	88	45	
		$2_1^+$	$0.24\pm 0.09$	$3.3 \times 10^{-5}$	0.052	0.038	

the one-body  $E2$  operator (17), e.g., the 3D-IBM results

TABLE V. Same as in the caption to Table IV but for the Pt nuclei.

	$I_i$	$I_f$	EXP	$\beta\gamma$	$\alpha\beta$	$\alpha\beta\gamma$
$^{192}\text{Pt}$	$2_1^+$	$0_1^+$	$57.2\pm 1.2$	59	59	60
		$4_1^+$	$89\pm 5$	82	83	83
		$6_1^+$	$70\pm 30$	89	90	91
		$2_2^+$	$109\pm 7$	39	44	44
		$0_1^+$	$0.55\pm 0.04$	2.7	2.2	2.4
	$3_1^+$	$4_1^+$	$38\pm 10$	25	18	25
		$2_2^+$	$102\pm 10$	80	61	79
		$2_1^+$	$0.68\pm 0.07$	4.1	3.5	3.6
	$4_2^+$	$4_1^+$		21	27	24
		$2_2^+$		29	44	33
		$2_1^+$		0.097	0.0021	0.054
		$0_2^+$	$2_2^+$	26	6.4	0.45
		$2_1^+$	1.8	3.3	3.0	
	$0_3^+$	$2_2^+$	0.47	74	0.002	
		$2_1^+$	0.14	2.2	0.40	
$^{194}\text{Pt}$	$2_1^+$	$0_1^+$	$49.2\pm 0.8$	48	48	48
		$4_1^+$	$85\pm 5$	63	64	65
		$6_1^+$	$67\pm 21$	67	68	70
		$2_2^+$	$89\pm 11$	61	64	63
		$0_1^+$	$0.29\pm 0.04$	0.072	0.052	0.056
	$3_1^+$	$4_1^+$		27	19	27
		$2_2^+$		62	49	63
		$2_1^+$		0.11	0.077	0.084
	$4_2^+$	$4_1^+$	14	15	32	23
		$2_2^+$	$21\pm 4$	20	36	29
		$2_1^+$	$0.36\pm 0.07$	0.0044	$1.1 \times 10^{-5}$	0.0036
	$0_2^+$	$2_2^+$	$8.4\pm 1.9$	27	0.12	0.016
	$2_1^+$	$0.63\pm 0.14$	0.060	2.2	2.8	
$0_3^+$	$2_2^+$		0.11	68	34	
	$2_1^+$		0.0082	0.065	0.052	
	$0_4^+$	$2_2^+$	$14.3\pm 1.4$	0.015	0.056	0.0043
		$2_1^+$	$14.1\pm 1.2$	0.44	0.21	0.042
$^{196}\text{Pt}$	$2_1^+$	$0_1^+$	$40.60\pm 0.20$	37	36	37
		$4_1^+$	$60.0\pm 0.9$	48	48	48
		$6_1^+$	$73^{+4}_{-73}$	50	50	51
		$2_2^+$		47	48	48
		$0_1^+$	$(4\pm 4) \times 10^{-6}$	0.036	0.021	0.023
	$3_1^+$	$4_1^+$		18	14	17
		$2_2^+$		43	35	43
		$2_1^+$		0.049	0.031	0.034
	$4_2^+$	$4_1^+$	$17\pm 6$	18	23	20
		$2_2^+$	$29^{+6}_{-29}$	22	26	23
		$2_1^+$	$0.56^{+0.12}_{-0.17}$	0.0042	$5.0 \times 10^{-4}$	0.0020
	$0_2^+$	$2_2^+$	$18\pm 10$	28	0.078	0.032
	$2_1^+$	$2.8\pm 1.5$	0.044	2.4	2.8	
$0_3^+$	$2_2^+$	$< 0.41$	0.011	49	33	
	$2_1^+$	$< 5.0$	0.0073	0.043	0.040	

for the  $E2$  transitions of the  $0_2^+$  states in both  $^{128}\text{Xe}$  and  $^{130}\text{Xe}$ . Nevertheless, it appears that the two-body  $E2$  operator does not improve dramatically the overall description of  $B(E2)$  transition probabilities. One should also note that the experimental results for these transitions have very large error bars.

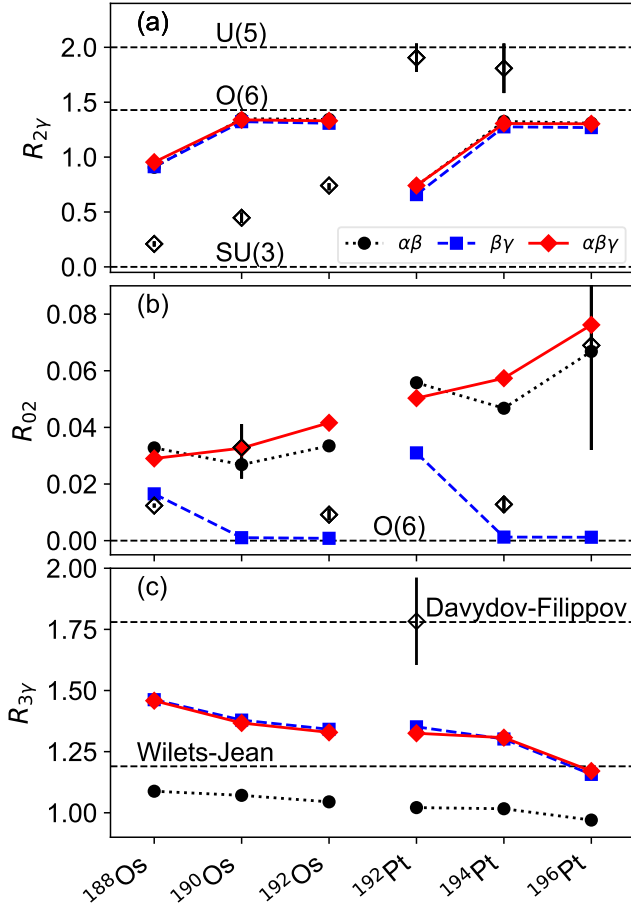


FIG. 13. The  $B(E2)$  ratios (a)  $R_{2\gamma} \equiv B(E2; 2_{\gamma}^{+} \rightarrow 2_{g}^{+})/B(E2; 2_{g}^{+} \rightarrow 0_{g}^{+})$ , (b)  $R_{02} \equiv B(E2; 0_{2}^{+} \rightarrow 2_{g}^{+})/B(E2; 2_{g}^{+} \rightarrow 0_{g}^{+})$ , and (c)  $R_{3\gamma} \equiv B(E2; 3_{\gamma}^{+} \rightarrow 2_{g}^{+})/B(E2; 2_{g}^{+} \rightarrow 0_{g}^{+})$  for  $^{188,190,182}\text{Os}$  and  $^{192,194,196}\text{Pt}$ . The IBM calculation is based on the PC-PK1 functional. The dynamical symmetry limits are indicated in panels (a) and (b). In panel (c), the geometrical limits of the Willets-Jean  $R_{3\gamma} = 1.19$ , and the Davydov-Filippov models  $R_{3\gamma} = 1.78$  are denoted by dashed lines. Experimental results are taken from [60], and are represented by the open symbols.

Similar observations can be made for the Os (Table IV) and Pt (Table V) nuclei. That is, the inclusion of dynamical pairing has a major effect on those  $B(E2)$  values that are related to the  $0_{2}^{+}$  state, while triaxiality leads to a better description of the  $E2$  rates for  $\gamma$ -band states. For all Os and Pt nuclei except  $^{194}\text{Pt}$ , in the 3D-IBM calculations the second  $4^{+}$  state corresponds to the  $I = 4^{+}$  member of the  $\gamma$ -vibrational band. Therefore, for the nucleus  $^{194}\text{Pt}$ , in Table V the 3D results for the  $B(E2; 4_{3}^{+} \rightarrow I_f)$  transition rates are compared with the experimental  $B(E2; 4_{2}^{+} \rightarrow I_f)$  values.

An empirical fact for  $\gamma$ -soft nuclei is that the  $B(E2; 2_{2}^{+} \rightarrow 2_{1}^{+})$  value is large and of the same order of magnitude as the  $B(E2; 2_{1}^{+} \rightarrow 0_{1}^{+})$ . For the Os iso-

topes, all three IBM calculations considerably overestimate the experimental  $B(E2; 2_{2}^{+} \rightarrow 2_{1}^{+})$  values. For the Pt isotopes, in turn, the corresponding  $B(E2; 2_{2}^{+} \rightarrow 2_{1}^{+})$  values are considerably smaller than those predicted for the Os nuclei. This discrepancy can be related to the result for the excitation spectra shown in Fig. 6, namely, that the  $2_{2}^{+}$  band-head of the  $\gamma$ -band is systematically overestimated in Pt. In addition, there is no significant difference in the  $B(E2; 2_{2}^{+} \rightarrow 2_{1}^{+})$  values predicted by the three IBM calculations, because the calculation suggests that both the ground state and  $\gamma$  bands predominantly belong to the normal  $[n_0]$  configuration.

In the O(6) limit of the IBM, the  $0_{2}^{+}$  state is interpreted to belong to the same  $\sigma = n_0$  family as the ground-state band, with the O(5) quantum number  $\tau = 3$ . Especially for the heavier nuclei considered, e.g.,  $^{192}\text{Os}$  and  $^{196}\text{Pt}$ , the measured  $E2$  transition rates show the pattern that is close to the O(6) prediction, characterized by the large  $B(E2; 0_{2}^{+} \rightarrow 2_{2}^{+})/B(E2; 0_{2}^{+} \rightarrow 2_{1}^{+})$  ratio. As seen from Table IV and Table V, the 2D- $\beta\gamma$  calculations for these nuclei provide results that exhibit this  $E2$  selection rule and that are in agreement with data. However, by the inclusion of the pairing the  $B(E2; 0_{2}^{+} \rightarrow 2_{2}^{+})$  transition rates are lowered by two orders of magnitude in most of the Os and Pt nuclei, while the  $B(E2; 0_{2}^{+} \rightarrow 2_{1}^{+})$  rates are increased, leading to the almost vanishing  $B(E2; 0_{2}^{+} \rightarrow 2_{2}^{+})/B(E2; 0_{2}^{+} \rightarrow 2_{1}^{+})$  ratio. In the 2D- $\alpha\beta$  and 3D- $\alpha\beta\gamma$  calculations the  $0_{2}^{+}$  states are dominated by the pair vibrational configurations (see, Fig. 9) for all the nuclei and, consequently, do not follow the  $E2$  selection rule that is expected by the O(6) symmetry. It appears, therefore, that the  $0_{2}^{+}$  states obtained by the present calculations that involve the pairing degree of freedom should not be associated with the  $0_{2}^{+}$  state in the O(6) limit. In fact, the  $0_{3}^{+}$  states for  $^{192}\text{Os}$  and  $^{196}\text{Pt}$  obtained from the 3D- $\alpha\beta\gamma$  as well as 2D- $\alpha\beta$  calculation, which are mainly composed of the normal configuration (Fig. 9), in turn, exhibit large  $B(E2; 0_{3}^{+} \rightarrow 2_{2}^{+})/B(E2; 0_{3}^{+} \rightarrow 2_{1}^{+})$  ratio, which is expected in the O(6) symmetry for the  $0_{2}^{+}$  state.

Some  $B(E2)$  values can be used as quantitative measures that differentiate between various limits of dynamical symmetries of the IBM and/or of the geometrical models of  $\gamma$ -soft nuclei. Figure 13 depicts the calculated  $B(E2)$  ratios (a)  $R_{2\gamma} \equiv B(E2; 2_{\gamma}^{+} \rightarrow 2_{g}^{+})/B(E2; 2_{g}^{+} \rightarrow 0_{g}^{+})$ , (b)  $R_{02} \equiv B(E2; 0_{2}^{+} \rightarrow 2_{g}^{+})/B(E2; 2_{g}^{+} \rightarrow 0_{g}^{+})$ , and (c)  $R_{3\gamma} \equiv B(E2; 3_{\gamma}^{+} \rightarrow 2_{g}^{+})/B(E2; 2_{g}^{+} \rightarrow 0_{g}^{+})$  for Os and Pt nuclei. In Fig. 13(a), the computed ratios  $R_{2\gamma}$  from all the three IBM calculations are close to the  $\gamma$ -unstable O(6) limit  $R_{2\gamma} = 10/7$ , both for Os and Pt. One notices that, in fact, for the Os nuclei this is at variance with the data, which are closer to the rotational SU(3) limit  $R_{2\gamma} = 0$ . This can be attributed to the fact that the SCMF-PESs suggest pronounced  $\gamma$ -softness in the Os chain. The values of the calculated ratio  $R_{02}$ , depicted in Fig. 13(b), are relatively small  $< 0.1$ . In particular, this is the case for the 2D- $\beta\gamma$  IBM results that are close to the experimental values and the O(6) limit  $R_{02} = 0$ . The

inclusion of the pairing degree of freedom does not seem to improve the description of this quantity. The ratio  $R_{3\gamma}$  differentiates between the rigid-triaxial-rotor and  $\gamma$ -unstable-rotor (equivalent to O(6) limit of the IBM) limits. With the restriction to axial symmetry in the 2D- $\alpha\beta$  calculations, this ratio is below the Willets-Jean limit of  $R_{3\gamma} = 1.19$ . The inclusion of triaxiality in the 2D- $\beta\gamma$  and 3D- $\alpha\beta\gamma$  IBM calculations, leads to an increase of the  $R_{3\gamma}$  ratio, such that it lies between the two geometrical limits.

TABLE VI. Comparison between the experimental [63] and theoretical  $\rho^2(E0; I_i \rightarrow I_f) \times 10^3$  values. The theoretical values are obtained from IBM calculations that include triaxial quadrupole (denoted by  $\beta\gamma$ ), axial plus dynamical pairing ( $\alpha\beta$ ), and triaxial plus dynamical pairing ( $\alpha\beta\gamma$ ) degrees of freedom. The IBM calculations are based on the PC-PK1 energy density functional.

	$I_i \rightarrow I_f$	EXP	$\beta\gamma$	$\alpha\beta$	$\alpha\beta\gamma$
$^{188}\text{Os}$	$0_2^+ \rightarrow 0_1^+$	$0.013 \pm 0.005$	0.00027	0.30	0.013
	$2_2^+ \rightarrow 2_1^+$	$0.7 \pm 0.6$	0.027	0.48	0.056
$^{194}\text{Pt}$	$0_2^+ \rightarrow 0_1^+$	$0.16 \pm 0.08$	0.0052	0.45	0.16
	$0_4^+ \rightarrow 0_1^+$	$11 \pm 4$	47	42	36
$^{196}\text{Pt}$	$2_2^+ \rightarrow 2_1^+$	$0.46 \pm 0.16$	0.011	0.036	0.018
	$0_2^+ \rightarrow 0_1^+$	$< 0.07$	0.34	0.47	0.31
	$0_3^+ \rightarrow 0_1^+$	$< 18$	17	0.61	0.61
	$0_3^+ \rightarrow 0_2^+$	$< 39$	0.069	0.0048	0.00025
	$2_2^+ \rightarrow 2_1^+$	$1.0 \pm 0.6$	0.022	0.025	0.019

### 3. $E0$ transition properties

Table VI lists the  $\rho^2(E0)$  values for  $^{188}\text{Os}$ ,  $^{194}\text{Pt}$ , and  $^{196}\text{Pt}$ , for which limited experimental results are available. The theoretical values are the results of IBM calculations including triaxial quadrupole ( $\beta\gamma$ ), axial plus dynamical pairing ( $\alpha\beta$ ), and triaxial plus dynamical pairing ( $\alpha\beta\gamma$ ) degrees of freedom. As one notices from the 2D- $\alpha\beta$ , and the 3D- $\alpha\beta\gamma$  results, the inclusion of triaxiality generally decreases the  $\rho^2(E0)$  values. The 2D- $\alpha\beta$  results are in better agreement with the experimental values, compared to the ( $\beta$ ,  $\gamma$ ) ones. Thus the pairing degree of freedom appears to be more important than triaxiality in describing  $E0$  transitions. However, because of a complex interplay between both degrees of freedom and also due to the presence of adjustable parameters in the  $E0$  operator, it is not straightforward to draw a generic conclusion about the relevance of considering both triaxial and pairing deformations in the calculation of the  $E0$  properties. For similar reasons, and also because of the present assignment of the  $0_2^+$  states to be mainly of pair-vibrational nature, the  $\rho^2(E0; 0_2^+ \rightarrow 0_1^+)$  value for  $^{196}\text{Pt}$ , which should vanish in the O(6) limit, is calculated to be much larger than the upper limit of the corresponding experimental value.

Figure 14 displays the  $\rho^2(E0; 0_2^+ \rightarrow 0_1^+) \times 10^3$  values and the  $X(E0/E2)$  ratios for the  $0_2^+ \rightarrow 0_1^+$  and  $0_3^+ \rightarrow 0_1^+$

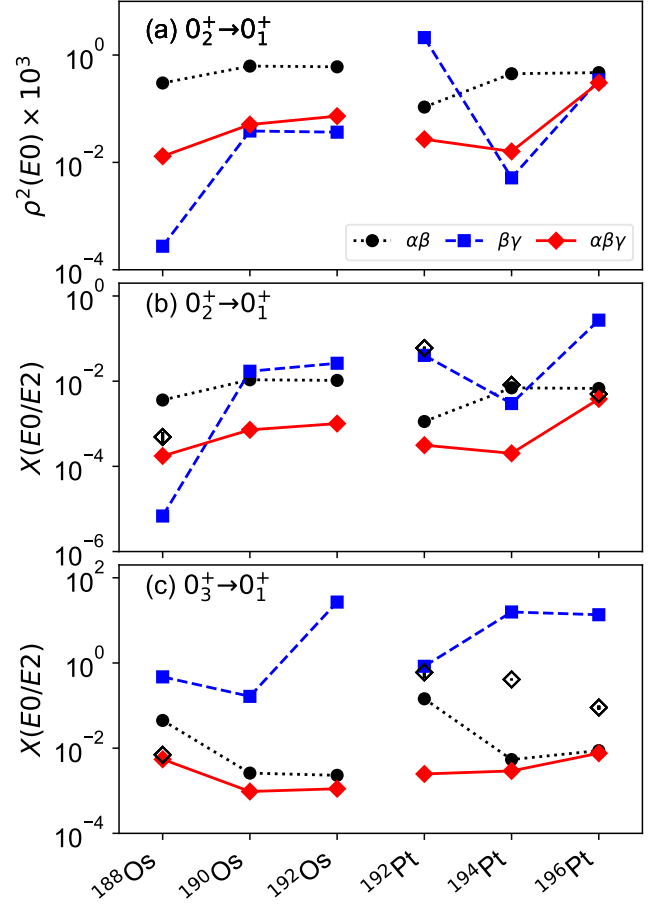


FIG. 14. The  $\rho^2(E0; 0_2^+ \rightarrow 0_1^+)$  values and  $X(E0/E2)$  ratios for the  $0_2^+ \rightarrow 0_1^+$  and  $0_3^+ \rightarrow 0_1^+$  transitions, for  $^{188,190,182}\text{Os}$  and  $^{192,194,196}\text{Pt}$ . The PC-PK1 functional is used in the IBM calculations. The experimental values are taken from [60, 64] for the  $X(E0/E2)$  ratios, and are represented by the open symbols.

transitions. The mixing ratio  $X(E0/E2)$  reads

$$X(E0/E2) = \frac{\rho^2(E0; 0_i^+ \rightarrow 0_f^+)e^2R^4}{B(E2; 0_i^+ \rightarrow 2_1^+)} \quad (22)$$

with  $R = 1.2A^{1/3}$  fm. As shown in Fig. 14, the considered  $E0$  transition properties are quite sensitive to the nature of the  $0^+$  states, and hence can differ by orders of magnitude between neighboring isotopes. For the  $X(E0/E2)$  ratios, in particular, the  $B(E2; 0_i^+ \rightarrow 2_1^+)$  value in the denominator is, in some cases, negligible, resulting in an unusually large mixing ratio. The simultaneous inclusion of triaxial and pairing deformations tends to result in a  $\rho^2(E0; 0_2^+ \rightarrow 0_1^+)$  value that is the smallest among the three types of IBM calculations, except for  $^{192}\text{Pt}$ . From both Figs. 14(b) and 14(c), one notices that the  $X(E0/E2)$  results obtained with the 3D- $\alpha\beta\gamma$  IBM, are the smallest among the three different calculations. The



same trend is observed in the  $X(E0/E2)$  results obtained with the DD-PC1 EDF.

## V. CONCLUSIONS

Based on the framework of nuclear EDFs, the effects of coupling between quadrupole triaxial shape and dynamical pairing degrees of freedom have been investigated in spectroscopic calculations of low-energy collective states of  $\gamma$ -soft nuclei. Constrained SCMF calculations have been performed using the RMF+BCS method with a choice of universal EDF and pairing interaction, resulting in potential energy surfaces as functions of the triaxial quadrupole  $(\beta, \gamma)$  and pairing  $\alpha$  degrees of freedom (the coordinate  $\alpha$  is proportional to the pairing gap  $\Delta$ ) for typical  $\gamma$ -soft nuclei in the mass  $A \approx 130$  ( $^{128,130}\text{Xe}$ ) and  $A \approx 190$  ( $^{188,190,192}\text{Os}$  and  $^{192,194,196}\text{Pt}$ ) regions.

The SCMF deformation energy surfaces for all considered nuclei exhibit notable softness in  $\alpha$  and  $\gamma$ , thus pointing to the importance of correlations that arise from fluctuations of triaxial and pairing deformations. Spectroscopic properties have been computed by employing the boson-number non-conserving IBM Hamiltonian, consisting of up to three-body boson terms. The parameters of the IBM Hamiltonian have been determined by mapping the SCMF-PES onto the expectation value of the Hamiltonian in the boson condensate state. The mapped IBM framework that simultaneously takes into account the dynamical pairing and quadrupole triaxial degrees of freedom has shown that: (i) the inclusion of dynamical pairing significantly lowers the energies of the excited  $0^+$  states and structures built on them, in good agreement with experimental results; (ii) the description

of  $\gamma$ -vibrational bands and the related  $B(E2)$  rates is considerably improved by the effect of triaxiality; and (iii) the principal results are not particularly sensitive to the choice of the microscopic EDF.

The results of the present work, together with those of the exploratory study for  $^{128,130}\text{Xe}$  [29], clearly demonstrate the importance of simultaneously including the dynamical pairing and quadrupole triaxial shape degrees of freedom, and their explicit coupling, for a quantitative description of low-energy collective states of medium-mass and heavy nuclei. The method developed here and in the previous work, can be used to explore interesting structure phenomena, such as shape phase transitions and shape coexistence in  $\gamma$ -soft and triaxial nuclei, in which cases both pairing vibrations and triaxial deformations are expected to play a significant role.

## ACKNOWLEDGMENTS

This work has been supported by the Tenure Track Pilot Programme of the Croatian Science Foundation and the École Polytechnique Fédérale de Lausanne, and the Project TTP-2018-07-3554 Exotic Nuclear Structure and Dynamics, with funds of the Croatian-Swiss Research Programme. It has also been supported in part by the QuantiXLie Centre of Excellence, a project co-financed by the Croatian Government and European Union through the European Regional Development Fund - the Competitiveness and Cohesion Operational Programme (KK.01.1.1.01.0004). The author Z.P.L. acknowledges support by the NSFC under Grant No. 11875225. The author J.X. acknowledges support by the NSFC under Grants No. 12005109 and No. 11765015.

- 
- [1] A. Bohr and B. R. Mottelson, *Nuclear Structure*, Vol. II (Benjamin, New York, USA, 1975).
  - [2] P. Cejnar, J. Jolie, and R. F. Casten, *Rev. Mod. Phys.* **82**, 2155 (2010).
  - [3] K. Heyde and J. L. Wood, *Rev. Mod. Phys.* **83**, 1467 (2011).
  - [4] P. Ring and P. Schuck, *The Nuclear Many-Body Problem* (Springer-Verlag, Berlin, 1980).
  - [5] F. Iachello and A. Arima, *The interacting boson model* (Cambridge University Press, Cambridge, 1987).
  - [6] M. Bender, P.-H. Heenen, and P.-G. Reinhard, *Rev. Mod. Phys.* **75**, 121 (2003).
  - [7] E. Caurier, G. Martínez-Pinedo, F. Nowacki, A. Poves, and A. P. Zuker, *Rev. Mod. Phys.* **77**, 427 (2005).
  - [8] T. Nikšić, D. Vretenar, and P. Ring, *Prog. Part. Nucl. Phys.* **66**, 519 (2011).
  - [9] N. Shimizu, T. Abe, Y. Tsunoda, Y. Utsuno, T. Yoshida, T. Mizusaki, M. Honma, and T. Otsuka, *Prog. Theor. Exp. Phys.* **2012**, 10.1093/ptep/pts012 (2012), 01A205, <https://academic.oup.com/ptep/article-pdf/2012/1/01A205/11585951/pts012.pdf>.
  - [10] D. R. Bès and R. A. Broglia, *Nucl. Phys.* **80**, 289 (1966).
  - [11] D. R. Bès, R. A. Broglia, R. P. J. Perazzo, and K. Kumar, *Nucl. Phys. A* **143**, 1 (1970).
  - [12] D. R. Bès, R. A. Broglia, and B. Nilsson, *Phys. Lett. B* **40**, 338 (1972).
  - [13] D. M. Brink and R. A. Broglia, *Nuclear superfluidity: pairing in finite systems* (Cambridge University Press, Cambridge, 2005).
  - [14] P. E. Garrett, *J. Phys. G: Nucl. Part. Phys.* **43**, 084002 (2016).
  - [15] D. R. Bès, *Nucl. Phys.* **49**, 544 (1963).
  - [16] D. R. Bès and C. Yi-Chung, *Nucl. Phys.* **86**, 581 (1966).
  - [17] R. F. Casten, E. R. Flynn, J. D. Garrett, O. Hansen, T. J. Mulligan, D. R. Bess, R. A. Broglia, and B. Nilsson, *Phys. Lett. B* **40**, 333 (1972).
  - [18] I. Ragnarsson and R. A. Broglia, *Nucl. Phys. A* **263**, 315 (1976).
  - [19] L. Próchniak, K. Zając, K. Pomorski, S. G. Rohoziński, and J. Srebrny, *Nucl. Phys. A* **648**, 181 (1999).
  - [20] J. Srebrny, T. Czosnyka, C. Droste, S. G. Rohoziński, L. Próchniak, K. Zając, K. Pomorski, D. Cline, C. Y. Wu,

- A. Bäcklin, L. Hasselgren, R. M. Diamond, D. Habs, H. J. Körner, F. S. Stephens, C. Baktash, and R. P. Kosteccki, *Nucl. Phys. A* **766**, 25 (2006).
- [21] L. Próchniak, *Int. J. Mod. Phys. E* **16**, 352 (2007).
- [22] N. L. Vaquero, T. R. Rodríguez, and J. L. Egido, *Phys. Rev. Lett.* **111**, 142501 (2013).
- [23] S. A. Giuliani, L. M. Robledo, and R. Rodríguez-Guzmán, *Phys. Rev. C* **90**, 054311 (2014).
- [24] J. Zhao, B.-N. Lu, T. Nikšić, D. Vretenar, and S.-G. Zhou, *Phys. Rev. C* **93**, 044315 (2016).
- [25] R. Rodríguez-Guzmán and L. M. Robledo, *Phys. Rev. C* **98**, 034308 (2018).
- [26] Rodríguez-Guzmán, R., Humadi, Y. M., and Robledo, L. M., *Eur. Phys. J. A* **56**, 43 (2020).
- [27] J. Xiang, Z. P. Li, T. Nikšić, D. Vretenar, and W. H. Long, *Phys. Rev. C* **101**, 064301 (2020).
- [28] K. Nomura, D. Vretenar, Z. P. Li, and J. Xiang, *Phys. Rev. C* **102**, 054313 (2020).
- [29] K. Nomura, D. Vretenar, Z. P. Li, and J. Xiang, *Phys. Rev. C* **103**, 054322 (2021).
- [30] J. Xiang, Z. P. Li, Z. X. Li, J. M. Yao, and J. Meng, *Nucl. Phys. A* **873**, 1 (2012).
- [31] P. W. Zhao, Z. P. Li, J. M. Yao, and J. Meng, *Phys. Rev. C* **82**, 054319 (2010).
- [32] T. Nikšić, D. Vretenar, and P. Ring, *Phys. Rev. C* **78**, 034318 (2008).
- [33] K. Nomura, T. Nikšić, T. Otsuka, N. Shimizu, and D. Vretenar, *Phys. Rev. C* **84**, 014302 (2011).
- [34] K. Nomura, N. Shimizu, D. Vretenar, T. Nikšić, and T. Otsuka, *Phys. Rev. Lett.* **108**, 132501 (2012).
- [35] J. F. Berger, M. Girod, and D. Gogny, *Nucl. Phys. A* **428**, 23 (1984).
- [36] S. Goriely, S. Hilaire, M. Girod, and S. Péru, *Phys. Rev. Lett.* **102**, 242501 (2009).
- [37] K. Nomura, T. Otsuka, R. Rodríguez-Guzmán, L. M. Robledo, and P. Sarriguren, *Phys. Rev. C* **83**, 014309 (2011).
- [38] K. Nomura, T. Otsuka, R. Rodríguez-Guzmán, L. M. Robledo, P. Sarriguren, P. H. Regan, P. D. Stevenson, and Z. Podolyák, *Phys. Rev. C* **83**, 054303 (2011).
- [39] K. Nomura, T. Otsuka, R. Rodríguez-Guzmán, L. M. Robledo, and P. Sarriguren, *Phys. Rev. C* **84**, 054316 (2011).
- [40] X. Q. Yang, L. J. Wang, J. Xiang, X. Y. Wu, and Z. P. Li, *Phys. Rev. C* **103**, 054321 (2021).
- [41] R. Casten and J. Cizewski, *Nucl. Phys. A* **309**, 477 (1978).
- [42] J. A. Cizewski, R. F. Casten, G. J. Smith, M. L. Stelts, W. R. Kane, H. G. Börner, and W. F. Davidson, *Phys. Rev. Lett.* **40**, 167 (1978).
- [43] Y. Tian, Z. Y. Ma, and P. Ring, *Phys. Lett. B* **676**, 44 (2009).
- [44] K. Nomura, N. Shimizu, and T. Otsuka, *Phys. Rev. Lett.* **101**, 142501 (2008).
- [45] K. Nomura, N. Shimizu, and T. Otsuka, *Phys. Rev. C* **81**, 044307 (2010).
- [46] T. Otsuka, A. Arima, and F. Iachello, *Nucl. Phys. A* **309**, 1 (1978).
- [47] P. Van Isacker and J.-Q. Chen, *Phys. Rev. C* **24**, 684 (1981).
- [48] K. Heyde, P. Van Isacker, M. Waroquier, and J. Moreau, *Phys. Rev. C* **29**, 1420 (1984).
- [49] J. N. Ginocchio and M. W. Kirson, *Nucl. Phys. A* **350**, 31 (1980).
- [50] A. E. L. Dieperink, O. Scholten, and F. Iachello, *Phys. Rev. Lett.* **44**, 1747 (1980).
- [51] A. Bohr and B. R. Mottelson, *Physica Scripta* **22**, 468 (1980).
- [52] A. Frank, P. Van Isacker, and C. E. Vargas, *Phys. Rev. C* **69**, 034323 (2004).
- [53] K. Nomura, R. Rodríguez-Guzmán, and L. M. Robledo, *Phys. Rev. C* **87**, 064313 (2013).
- [54] K. Nomura, R. Rodríguez-Guzmán, and L. M. Robledo, *Phys. Rev. C* **94**, 044314 (2016).
- [55] K. Nomura, T. Otsuka, and P. V. Isacker, *Journal of Physics G: Nuclear and Particle Physics* **43**, 024008 (2016).
- [56] J. E. García-Ramos and K. Heyde, *Phys. Rev. C* **100**, 044315 (2019).
- [57] K. Nomura, T. Otsuka, N. Shimizu, and L. Guo, *Phys. Rev. C* **83**, 041302 (2011).
- [58] D. R. Inglis, *Phys. Rev.* **103**, 1786 (1956).
- [59] S. T. Beliaev, *Nucl. Phys.* **24**, 322 (1961).
- [60] Brookhaven National Nuclear Data Center, <http://www.nndc.bnl.gov>.
- [61] A. S. Davydov and G. F. Filippov, *Nucl. Phys.* **8**, 237 (1958).
- [62] L. Wilets and M. Jean, *Phys. Rev.* **102**, 788 (1956).
- [63] J. Wood, E. Zganjar, C. De Coster, and K. Heyde, *Nuclear Physics A* **651**, 323 (1999).
- [64] T. Kibédi and R. Spear, *At. Data and Nucl. Data Tables* **89**, 77 (2005).